Astronomy & Astrophysics manuscript no. SN1987A
March 2, 2022

Supernova 1987A: neutrino-driven explosions in three dimensions and light curves

V. P. Utrobin[1,2], A. Wongwathanarat[1,3], H.-Th. Janka[1], and E. Müller[1]

[1] Max-Planck-Institut für Astrophysik, Karl-Schwarzschild-Str. 1, 85748 Garching, Germany
[2] State Scientific Center of the Russian Federation – Institute for Theoretical and Experimental Physics of National Research Center "Kurchatov Institute", B. Cheremushkinskaya St. 25, 117218 Moscow, Russia
[3] RIKEN, Astrophysical Big Bang Laboratory, 2-1 Hirosawa, Wako, Saitama 351-0198, Japan

Received 13 December 2014 / accepted 8 June 2015

ABSTRACT

Context. The well-observed and well-studied type IIP Supernova 1987A (SN 1987A), produced by the explosion of a blue supergiant in the Large Magellanic Cloud, is a touchstone for the evolution of massive stars, the simulation of neutrino-driven explosions, and the modeling of light curves and spectra.
Aims. In the framework of the neutrino-driven explosion mechanism, we study the dependence of explosion properties on the structure of different blue supergiant progenitors and compare the corresponding light curves with observations of SN 1987A.
Methods. Three-dimensional (3D) simulations of neutrino-driven explosions are performed with the explicit, finite-volume, Eulerian, multifluid hydrodynamics code Prometheus, using of four available presupernova models as initial data. At a stage of almost homologous expansion, the hydrodynamical and composition variables of the 3D models are mapped to a spherically symmetric configuration, and the simulations are continued with the implicit, Lagrangian radiation-hydrodynamics code Crab to follow the blast-wave evolution into the SN outburst.
Results. All of our 3D neutrino-driven explosion models, with explosion energies compatible with SN 1987A, produce ^{56}Ni in rough agreement with the amount deduced from fitting the radioactively powered light-curve tail. Two of our models (based on the same progenitor) yield maximum velocities of around 3000 km s^{-1} for the bulk of ejected ^{56}Ni, consistent with observational data. In all of our models inward mixing of hydrogen during the 3D evolution leads to minimum velocities of hydrogen-rich matter below 100 km s^{-1}, which is in good agreement with spectral observations. However, the explosion of only one of the considered progenitors reproduces the shape of the broad light curve maximum of SN 1987A fairly well.
Conclusions. The considered presupernova models, 3D explosion simulations, and light-curve calculations can explain the basic observational features of SN 1987A, except for those connected to the presupernova structure of the outer stellar layers. All progenitors have presupernova radii that are too large to reproduce the narrow initial luminosity peak, and the structure of their outer layers is not suitable to match the observed light curve during the first 30–40 days. Only one stellar model has a structure of the helium core and the He/H composition interface that enables sufficient outward mixing of ^{56}Ni and inward mixing of hydrogen to produce a good match of the dome-like shape of the observed light-curve maximum, but this model falls short of the helium-core mass of 6 $M_\odot$ inferred from the absolute luminosity of the presupernova star. The lack of an adequate presupernova model for the well-studied SN 1987A is a real and pressing challenge for the theory of the evolution of massive stars.

Key words. hydrodynamics – instabilities – nucleosynthesis – shock waves – stars: supernovae: individual: SN 1987A – stars: supernovae: general

1. Introduction

It is well known that massive stars die as core-collapse supernovae (SNe). Type II-plateau supernovae (SNe IIP) represent the most numerous subclass of core-collapse SNe. They are characterized by a ∼100 day plateau in the light curve, which is a generic feature of the explosion of a red supergiant (RSG) star (Grassberg et al. 1971; Falk & Arnett 1977). The RSG nature of SNe IIP was confirmed by the detection of their progenitors on archival images (Smartt 2009). The theory of stellar evolution also predicts that stars in the range of $9 - 25...30\,M_\odot$ end their life as RSGs (Heger et al. 2003). In addition to the ordinary SNe IIP, there is a group of peculiar objects of which SN 1987A in the Large Magellanic Cloud (LMC) is the best studied. It was identified with the explosion of the blue supergiant (BSG) Sanduleak −69°202 and is a serious challenge for theorists.

We still have no clear answer to why its progenitor was a compact star. Just a couple of months after the discovery of SN 1987A, Arnett (1987) and Hillebrandt et al. (1987) showed that a metal-deficient composition similar to the LMC favors the formation of BSGs. It, however, cannot explain the high nitrogen abundance that was revealed in the circumstellar matter of SN 1987A by an analysis of ultraviolet lines (Cassatella 1987; Lundqvist & Fransson 1996). In addition, either a modification of convective mixing through rotation-induced meridional circulation in the star during its evolution (Weiss et al. 1988), a restricted semiconvective diffusion (Woosley et al. 1988), both mass loss and convective mixing (Saio et al. 1988), or invoking mass-loss effects in a close binary system (Hillebrandt & Meyer 1989; Podsiadlowski & Joss 1989) are required to fit the observed properties of Sanduleak −69°202 in evolutionary calculations.

The phenomenon of core-collapse SNe is very complex and how massive stars explode has only been elucidated in recent decades, but we still do not know exactly how the explosion engine works (Woosley & Janka 2005; Janka 2012; Janka et al. 2012; Burrows 2013). While this problem is difficult to solve for a variety of reasons, very different energies and timescales inside the star just before the gravitational collapse of its central iron core separate the evolution of the iron core from that of outer layers. These vast differences allow us to divide the whole problem into two: an internal problem (the gravitational collapse itself) and an external problem (the collapse-initiated SN outburst) (Imshennik & Nadezhin 1989), and to study them independently. We briefly present these two approaches focusing on the well-observed and well-studied peculiar SN 1987A. We start with the external problem, as it directly deals with the photometric and spectroscopic observations.

One of the surprises associated with SN 1987A was the observational evidence for macroscopic mixing occurring during the explosion. This kind of effect is required to reproduce both the smooth rising part of the bolometric light curve and the major broad maximum with a timescale of ∼100 days (Woosley 1988; Shigeyama & Nomoto 1990; Utrobin 1993). The smoothness of the bolometric light curve results from the mixing of radioactive ^{56}Ni out of the center, while the wide dome-like light curve maximum comes from mixing hydrogen-rich matter down to the center.

The extent of mixing of radioactive ^{56}Ni and hydrogen in the ejected envelope is a crucial point for understanding SN 1987A. Observational evidence for this mixing in the envelope exists not only at early times, but also at late times. At early times (during 20–100 days), the Hα profile exhibits a striking fine structure called "Bochum event" (Hanuschik & Dachs 1987; Phillips & Heathcote 1989). At day 410, a unique high velocity feature with a radial velocity of about +3900 km s^{-1} was found in the 17.9 and 26.0 μm infrared emission lines of [Fe II]. It was interpreted as a fast iron clump with a mass of $2 \times 10^{-3}\,M_{\odot}$ (Haas et al. 1990). Later, a similar high velocity feature was detected in the 6.6 μ infrared emission line of [Ni II] at day 640 (Colgan et al. 1994). Utrobin et al. (1995) analyzed the Hα profile at the Bochum event phase (days 29 and 41) and identified this high velocity feature with a fast ^{56}Ni clump that was moving at an absolute velocity of 4700 km s^{-1} and had a mass of $\sim 10^{-3}\,M_{\odot}$. As to the bulk of radioactive ^{56}Ni, measurements of the 6.6 μm infrared emission line of [Ni II] and the 17.9 and 26.0 μm lines of [Fe II] at day 640 showed that it was moving with a maximum velocity of ∼3000 km s^{-1} (Colgan et al. 1994).

The fact that the Hα profile observed by Phillips et al. (1990) at day 498 was not flat topped implies that there was no large cavity free of hydrogen at the center of the ejecta, but that hydrogen was mixed deeply down to a velocity of ∼500 km s^{-1}. Chugai (1991) investigated the profiles of hydrogen emission lines at day 350 and argued that the slowest moving hydrogen was observed at a velocity of ∼600 km s^{-1}. Kozma & Fransson (1998) analyzed the Hα profile taken at day 804 and found that hydrogen extended into the core to velocities ≤ 700 km s^{-1}. Thus, the presence of hydrogen within the core of heavy elements is confirmed by the observational data of SN 1987A.

The hydrodynamic models of SN 1987A based on evolutionary calculations of the pre-SN are consistent with the observed light curve when ^{56}Ni is artificially mixed up to velocities of ∼4000 km s^{-1} (Shigeyama & Nomoto 1990; Blinnikov et al. 2000; Utrobin 2004). On the other hand, the hydrodynamic simulations of the SN 1987A explosion based on nonevolutionary pre-SN models showed in agreement with observations that the bulk of ^{56}Ni is mixed up to velocities of 2500 km s^{-1} (Utrobin 1993, 2004). Photometric data of SN 1987A combined with spectra are the primary source of our knowledge of its properties. Atmosphere models with the steady-state approximation for the ionization kinetics produced a too weak Hα line compared to the observed line. After solving the problem of the Hα line strength at the photospheric phase in the framework of a time-dependent approach (Utrobin & Chugai 2002, 2005), it became possible to simultaneously fit the hydrodynamic and atmosphere models to both the photometric and spectroscopic observations with moderate ^{56}Ni mixing up to velocities of 3000 km s^{-1} (Utrobin 2005). To reproduce the broad light curve maximum with hydrodynamic models, Woosley (1988), Shigeyama & Nomoto (1990), Blinnikov et al. (2000), and Utrobin (2005) mixed hydrogen-rich matter down to velocities of about 1700, 800, 1300, and 600 km s^{-1}, respectively.

Besides the direct spectroscopic evidence for moderate ^{56}Ni mixing up to velocities of 3000 km s^{-1}, there are a number of indirect indications. Moderate ^{56}Ni mixing is supported by the modeling of infrared emission lines at late stages from 200 to 700 days. Li et al. (1993) showed that the intensity of iron, cobalt, and nickel emission lines and their evolution with time are consistent with ^{56}Ni mixing up to velocities of ∼2500 km s^{-1}, while the same observations led Kozma & Fransson (1998) to conclude that the iron synthesized during the explosion is mixed to velocities of 2000 km s^{-1}. Using Monte Carlo techniques for calculating the X-ray emission and the 847 and 1238 keV gamma-ray lines, Pinto & Woosley (1988) found that a fit to the observations required ^{56}Co mixing up to a velocity of 3000 km s^{-1}. In addition, Monte Carlo simulations of gamma-ray transport of the 847 and 1238 keV lines of ^{56}Co in the envelope showed that the velocity of up to 50% of the total ^{56}Ni mass should remain below 1000 km s^{-1} (Burrows & van Riper 1995).

These observational data obtained from SN 1987A unambiguously demonstrate that the envelope of the pre-SN was substantially fragmented during the explosion. These observations impose serious constraints on the internal problem of the SN explosion, and thus stimulated theoretical and numerical work on hydrodynamic instabilities, which followed two distinct approaches. On the one hand, multidimensional modeling of the explosion mechanism was attempted (Herant et al. 1992; Burrows & Fryxell 1993; Miller et al. 1993; Herant et al. 1994; Burrows et al. 1995; Janka & Müller 1996; Mezzacappa et al. 1998), mainly with the aim of answering the question as to which extent convective instabilities are helpful for generating neutrino-driven explosions. These simulations were confined to the early shock propagation phase up to about one second after core bounce.

On the other hand, hydrodynamic models of the late-time shock propagation and the associated formation of Rayleigh-Taylor instabilities in the expanding mantle and envelope of the exploding star (Arnett et al. 1989; Fryxell et al. 1991; Müller et al. 1991a,b; Hachisu et al. 1990, 1991, 1992, 1994; Yamada & Sato 1990, 1991; Herant & Benz 1991, 1992; Herant & Woosley 1994; Shigeyama et al. 1996; Iwamoto et al. 1997; Nagataki et al. 1998; Kane et al. 2000) ignored the complications of the explosion mechanism. Owing to considerable computational difficulties in resolving the relevant spatial and temporal scales, all of these investigations relied on ad hoc procedures to initiate the explosion. This usually meant that some simple form of energy deposition (by a piston or "thermal bomb") was used to generate a shock wave in a pre-SN model. The subsequent propagation of the blast wave was followed in a one-dimensional (1D) simulation until the shock had reached the (C+O)/He or the He/H in-

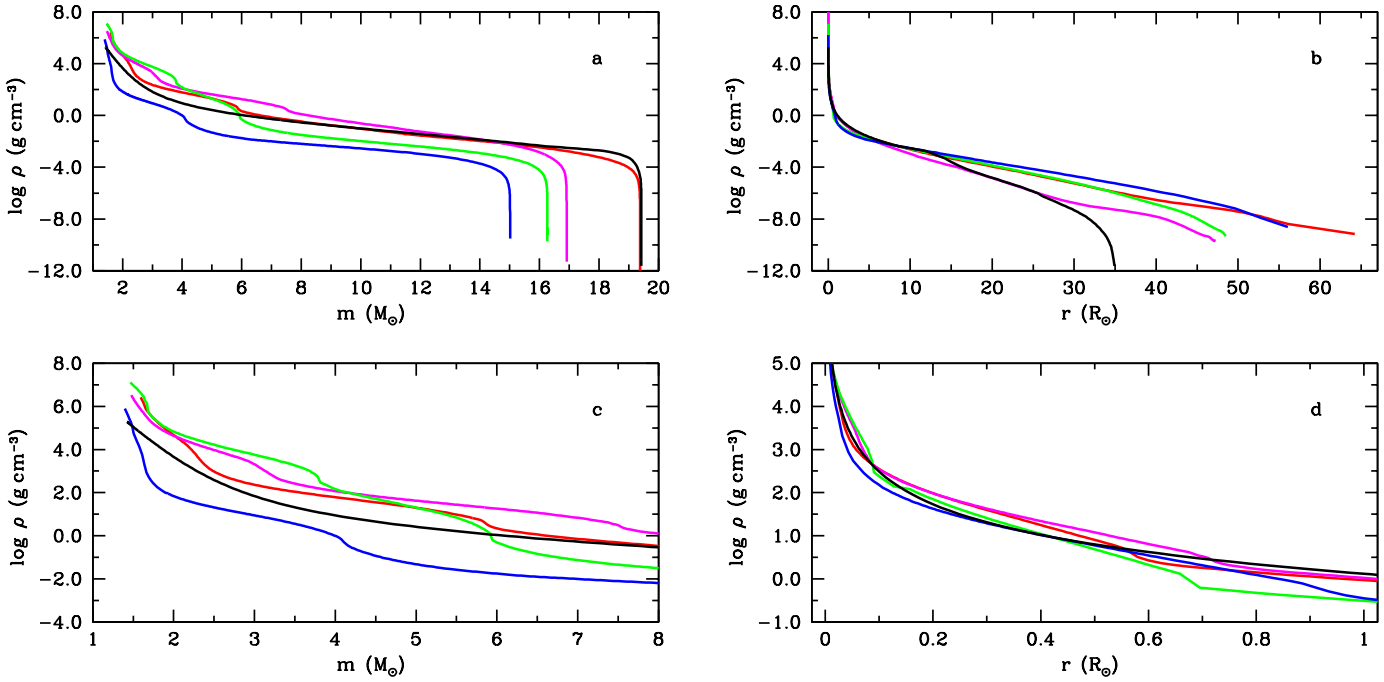

Fig. 1. Density distributions as functions of interior mass for the whole star (Panel **a**) and the inner region of 8 $M_\odot$ (Panel **c**) and as functions of radius for the whole star (Panel **b**) and the inner region of 1 $R_\odot$ (Panel **d**) in pre-SN models B15 (*blue line*), N20 (*green line*), W18 (*magenta line*), and W20 (*red line*). The central collapsing cores are omitted. For a comparison, the *black line* shows the structure of a nonevolutionary pre-SN model used by Utrobin (2005).

terface. Then, the 1D model was mapped to a multidimensional grid, and an assumed spectrum of seed perturbations was added to the radial velocity field to break the spherical symmetry of the problem and to trigger the growth of instabilities. Ellinger et al. (2012) somewhat improved the appoach of the studies mentioned above by starting 3D calculations shortly after the successful shock revival. The studies of Yamada & Sato (1990, 1991), Nagataki et al. (1997, 1998) and the three-dimensional (3D) calculations of Hungerford et al. (2003), who investigated the effects of metal mixing on X-ray and gamma-ray spectra formation, differ from this approach by making use of parameterized, aspherical shock waves.

All of the Rayleigh-Taylor simulations that had been carried out for reproducing the mixing in SN 1987A with spherically symmetric initiation of the explosion had shared the same problem: with at most 2000 km s^{-1} their maximum ^{56}Ni velocities were significantly smaller than the observed values of 3000 km s^{-1} for the bulk of radioactive ^{56}Ni. Herant & Benz (1992) dubbed this problem the "nickel discrepancy". They also speculated that it should disappear when the "premixing" of the ejecta during the phase of neutrino-driven convection is taken into account. On the other hand, Nagataki et al. (1998) did not agree with Herant & Benz. They claimed that the nickel discrepancy is resolved if the SN shock is (mildly) aspherical. Similar conclusions were reached by Hungerford et al. (2003). While Nagataki et al. as well as Hungerford et al. did not rule out neutrino-driven convection around the neutron star as an explanation for the assumed asphericity of their shocks, Khokhlov et al. (1999), Wheeler et al. (2002), and Wang et al. (2002) questioned the neutrino-driven mechanism. Instead, they speculated about "jet-driven" explosions, which might originate from magnetohydrodynamic effects in connection with a rapidly rotating neutron star.

The controversy described above demonstrated the need for models that link observable features at very large radii to the actual energy source and the mechanism of the explosion. Kifonidis et al. (2000, 2003, 2006) provided this link for the standard paradigm of neutrino-powered explosions in two-dimensional (2D) geometry. Their models included a detailed treatment of shock revival by neutrinos, the accompanying convection and nucleosynthesis, and the growth of Rayleigh-Taylor instabilities at the composition interfaces of the pre-SN star after shock passage. They employed high spatial resolution by making use of adaptive mesh refinement techniques, which is mandatory for highly detailed tracking of the episodes of clump formation, mixing, and clump propagation. Kifonidis et al. (2003) showed that the large asymmetries imprinted on the ejecta by the violent, nonradial mass motions in the SN core, which precede and accompany the neutrino-driven revival of the blast wave, seed the growth of secondary Rayleigh-Taylor instability in the shock-accelerated outer shells of the exploding star. Since the developing Rayleigh-Taylor mushrooms are denser than the surrounding gas, they are less decelerated than their environment and can penetrate the composition interfaces of the pre-SN star, retaining high velocities as the SN ejecta expand. Thus, they carry freshly synthesized radioactive ^{56}Ni and other heavy elements from the vicinity of the nascent neutron star into the outer stellar layers. Kifonidis et al. (2006) demonstrated that massive ^{56}Ni-dominated clumps can be mixed deep into the helium shell and even into the hydrogen layer of the disrupted star with terminal velocities of up to ~3000 km s^{-1}, solving the "nickel discrepancy" problem. In turn, hydrogen can be mixed at the He/H composition interface downward in velocity space to only 500 km s^{-1}. Recent 3D hydrodynamic simulations of neutrino-driven explosions, for SN 1987A as well, (Hammer et al. 2010; Wongwathanarat et al. 2010b; Müller et al. 2012b; Wongwathanarat et al. 2013, 2015) have confirmed the basic results of the

Table 1. Presupernova models for blue supergiants.

Model	$R_{\rm pSN}$ ($R_\odot$)	$M_{\rm He}^{\rm core}$ ($M_\odot$)	$M_{\rm pSN}$ ($M_\odot$)	$M_{\rm ZAMS}$ ($M_\odot$)	$X_{\rm surf}$	$Y_{\rm surf}$	$Z_{\rm surf}$ (10^{-2})	$\xi_{1.5}$	Ref
B15	56.1	4.05	15.02	15.02	0.767	0.230	0.34	0.24	1
N20	47.9	5.98	16.27	∼20.0	0.560	0.435	0.50	0.83	2
W18	46.8	7.40	16.92	18.0	0.480	0.515	0.50	0.68	3
W20	64.2	5.79	19.38	20.10	0.738	0.256	0.56	0.78	4

Notes. The columns give the name of the pre-SN model, its radius, $R_{\rm pSN}$; the helium-core mass, $M_{\rm He}^{\rm core}$; the pre-SN mass, $M_{\rm pSN}$; the progenitor mass, $M_{\rm ZAMS}$; the mass fraction of hydrogen, $X_{\rm surf}$; helium, $Y_{\rm surf}$; and heavy elements, $Z_{\rm surf}$, in the hydrogen-rich envelope at the stage of core collapse; the compactness parameter, $\xi_{1.5}$; and the corresponding reference.

References. (1) Woosley et al. (1988); (2) Shigeyama & Nomoto (1990); (3) Woosley (2007); (4) Woosley et al. (1997).

2D simulations in the context of radioactive ^{56}Ni and hydrogen mixing. Hammer et al. (2010), in particular, demonstrated that the initial explosion asymmetries can be less extreme in 3D than in 2D to explain high ^{56}Ni velocities in the hydrogen layer because drag forces lead to less deceleration of 3D metal clumps compared to 2D axisymmetric and, thus, toroidal structures. Recently, Handy et al. (2014) have shown that the convective engine, powering the standing accretion shock, is slightly more efficient in their 3D simulations than in 2D ones. Requiring the same explosion energy of their SN 1987A model, they needed a 4% lower luminosity for their neutrino light bulb in the 3D case than in the 2D case.

In this paper, we revisit the analysis of the peculiar SN 1987A by successively combining the capabilities of the internal and external problems. First, we carry out 3D hydrodynamic simulations of neutrino-driven explosions for a set of evolutionary models of the BSG Sanduleak −69°202 available to us. These simulations provide us with a complex morphology of radioactive ^{56}Ni and hydrogen mixing, which retains its global radial features after mapping to a spherically symmetric grid. Second, in spherically symmetric geometry we hydrodynamically model the SN 1987A outburst and its light curve. It is noteworthy that the obtained mixing of radioactive ^{56}Ni and hydrogen is more realistic than the artificial mixing used in all previous hydrodynamic studies of SN 1987A. The present study is a first attempt of a self-consistent modeling of the SN development from the revival of the stalled shock to the epoch of the radioactive tail of the light curve.

We begin in Sect. 2 with a brief description of the pre-SN models used in our study, the 3D hydrodynamic simulations, and the hydrodynamic light curve modeling. Section 3 analyzes the results obtained and compares them with SN 1987A observations. In Sect. 4 we discuss our results and their implications for the problem of the explosion mechanism, and in Sect. 5 we summarize and conclude.

2. Model overview

2.1. Presupernova models

We have analyzed a set of pre-SN models, B15, N20, W18, and W20 obtained for 15, 20, 18, and 20 $M_\odot$ progenitor stars evolved by Woosley et al. (1988), Shigeyama & Nomoto (1990), Woosley (2007), and Woosley et al. (1997), respectively (Table 1). These pre-SN models are used as the initial data in our 3D neutrino-driven simulations. All pre-SN models, except B15, are computed with mass loss. In contrast to the other models, model W18 results from the evolution of a rotating progenitor. Mass loss and rotation along with the metal-deficient composition of the LMC and the convective mixing favor the formation of BSG-like pre-SN models (Table 1).

O'Connor & Ott (2011) studied the spherically symmetric collapse of stellar cores by hydrodynamic simulations with a simplified neutrino treatment. In their study, O'Connor & Ott proposed that the fate of collapsing stars, successful explosion with neutron star formation or failing SN and black hole formation, can be predicted with a single parameter, the compactness of the pre-SN structure at core bounce, $\xi_{2.5}$, of the innermost 2.5 $M_\odot$ of a star. Sukhbold & Woosley (2014) showed that this parameter might be evaluated for the "presupernova model" defined by the moment when the collapse speed reaches 1000 km s^{-1}. They also compared the compactness values for different choices of the enclosed mass. It appears reasonable to assume that the 1.5 $M_\odot$ core of the pre-SN is more relevant in connection to the production of radioactive ^{56}Ni and its mixing compared to the value considered by O'Connor & Ott. For reference, we also give the compactness parameter $\xi_{1.5}$ for all of our pre-SN models in Table 1.

Saio et al. (1988) and Woosley (1988) showed that the luminosity of the BSG Sanduleak −69°202 is consistent with a star that had a helium core of ≈6 $M_\odot$ at the time of explosion. Models N20 and W20 match these pre-explosion observations of SN 1987A, but models B15 and W18 have a helium-core mass[1] quite different from the required value (Table 1, Figs. 1a and c). Kifonidis et al. (2006) and Wongwathanarat et al. (2015) found that the amount of outward ^{56}Ni mixing and inward hydrogen mixing is sensitive to the structure of the helium core and the He/H composition interface. The different helium cores in the mass range from 4 to 7.5 $M_\odot$ (Table 1) allow for a study of this sensitivity for BSG progenitors, which also differ in their density distributions versus radius (Figs. 1b and d) and chemical compositions (Fig. 2).

2.2. 3D neutrino-driven explosions

Our 3D simulations of supernova explosions are carried out with the explicit finite-volume, Eulerian, multifluid hydrodynamics code Prometheus (Fryxell et al. 1991; Müller et al. 1991a,b). It integrates the multidimensional hydrodynamic equations using dimensional splitting (Strang 1968), piecewise parabolic reconstruction (Colella & Woodward 1984), and a Riemann solver for real gases (Colella & Glaz 1985). Inside grid cells with strong grid-aligned shocks, fluxes computed with the Riemann solver are replaced by the AUSM+ fluxes of Liou (1996) to preclude odd-even decoupling (Quirk 1994). The code treats advection of nuclear species by employing the consistent multifluid advection scheme of Plewa & Müller (1999).

The code employs an axis-free overlapping "Yin-Yang" grid (Kageyama & Sato 2004) in spherical polar coordinates, which was implemented into Prometheus (Wongwathanarat et al. 2010a). The Yin-Yang grid relaxes the restrictive CFL-timestep condition and avoids numerical artifacts near the polar axis. Our standard grid configuration consists of $400(r)\times47(\theta)\times137(\phi)\times2$ grid cells, corresponding to an angular resolution of 2° and cov-

[1] We define the helium-core mass as the mass enclosed by the shell where the mass fraction of hydrogen X drops below a value of $X = 0.01$ when moving inward from the surface of a star (S. E. Woosley, private communication).

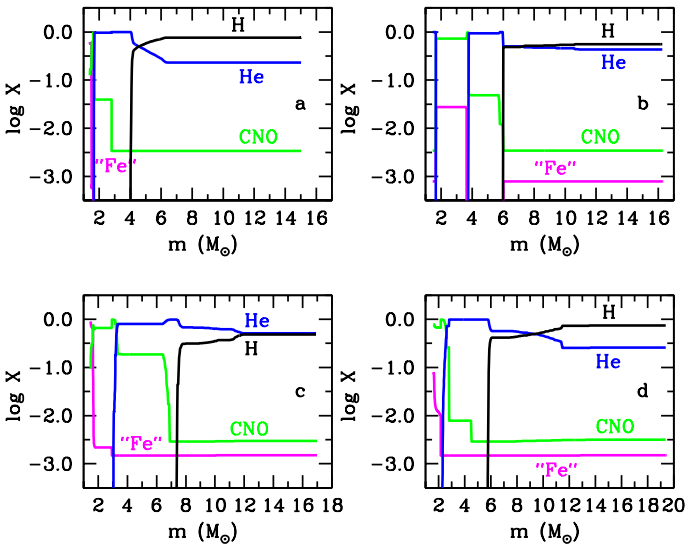

Fig. 2. Mass fractions of hydrogen (*black line*), helium (*blue line*), CNO group elements (*green line*), and iron group elements (*magenta line*) in the pre-SN models B15 (Panel **a**), N20 (Panel **b**), W18 (Panel **c**), and W20 (Panel **d**).

ering the full 4π solid angle. Depending on the evolution phase, hydrostatic equilibrium, a wind-inflow condition or an open outflow condition is assumed at the inner grid boundary, while a free outflow boundary condition is employed at the outer one at all times (see Wongwathanarat et al. 2015, for details).

We take self-gravity into account by solving Poisson's equation in its integral form, using an expansion into spherical harmonics (Müller & Steinmetz 1995). The monopole term of the potential is corrected for general relativistic effects as described by Scheck et al. (2006) and Arcones et al. (2007). The inner core of the proto-neutron star (PNS) with densities well above those of the neutrinospheric layer is excised and replaced by a point mass at the coordinate origin. The cooling of the excised part of the PNS is then described by neutrino emission properties (luminosities and mean spectral energies), which are prescribed as time-dependent boundary conditions. The contraction of the PNS is mimicked by a movement of the inner radial grid boundary. During evolutionary phases significantly later than one second after core collapse, the PNS is removed from the simulations and the inner grid boundary is placed at successively larger radii (cf. Wongwathanarat et al. 2015).

We approximate "ray-by-ray" neutrino transport and neutrino-matter interactions as in Scheck et al. (2006) by radial integration of the 1D (spherical), gray transport equation for ν_e, $\bar{\nu}_e$, and heavy-lepton neutrinos independently for all angular grid directions (θ, ϕ). This approach allows us to take angular variations of the neutrino fluxes produced by the matter accreted onto the newly forming NS into account. The accretion luminosity adds to the neutrino fluxes imposed spherically and symmetrically at the inner grid boundary. The neutrino spectra are assumed to have Fermi-Dirac shape with chemical potentials that are equal to the equilibrium values in optically thick regions and constant, limiting values in the free streaming regime. The spectral temperatures are computed from inverting the ratio of neutrino energy and number fluxes, whose transport is solved simultaneously. Details can be found in Scheck et al. (2006). The tabulated equation of state (EoS) of Janka & Müller (1996) is used to describe the stellar fluid. It includes arbitrarily degenerate and arbitrarily relativistic electrons and positrons, photons, and four predefined nuclear species (n, p, α, and a representative Fe-group nucleus) in nuclear statistical equilibrium.

To follow the explosive nucleosynthesis approximately, we solve a small α-chain reaction network, similar to the network described in Kifonidis et al. (2003). For our simulations we consider 13 α-nuclei from ^{4}He to ^{56}Ni and an additional "tracer nucleus". The tracer nucleus represents iron-group species that are formed under conditions of neutron excess in the neutrino-heated material. It is produced via the reaction ^{52}Fe(α,γ)^{56}Ni within grid cells whose electron fraction Y_e is below 0.49 in our simulations. The tracer thus allows us to keep track of nucleosynthesis in regions with neutron excess. However, it should be noted that some fraction of the tracer material may actually be ^{56}Ni because our approximations in the neutrino transport tend to underestimate Y_e in the neutrino-heated ejecta, while more sophisticated energy-dependent neutrino transport can also yield (slightly) proton-rich conditions in the neutrino-processed material expelled during the early explosion (e.g., Pruet et al. 2006; Fröhlich et al. 2006; Fischer et al. 2010; Müller et al. 2012a). The exact Y_e value of this SN ejecta component, however, remains a matter of vivid debate and sensitively depends on uncertain aspects of nuclear physics, neutrino reactions, and the dynamics of the collapsing stellar core (see, e.g., the review by Janka (2012) and new results by Tamborra et al. (2014)).

Since we are therefore unable to determine the ^{56}Ni production in our models very accurately, we provide maximum and minimum ^{56}Ni yields, depending on whether the tracer material is added to the explosively produced ^{56}Ni mass or not. The explosively assembled radioactive nickel originates from shock-heated ejecta and is computed with our nuclear network. A "representative" mass of radioactive ^{56}Ni is defined by all explosively made nickel plus 50% of the tracer mass (cf. Table 2).

The network is solved in grid cells whose temperature is within the range of 10^8 K – 8×10^9 K. We assume that all nuclei are photodisintegrated to α-particles at temperatures above $8{\times}10^9$ K. This is the high-temperature nuclear statistical equilibrium composition compatible with our α-network in the absence of free neutrons and protons. We neglect feedback from the detailed network composition to the EoS and the hydrodynamic flow. This is an acceptable approximation because at SN conditions the contributions of nuclei to pressure, energy density, and entropy are dwarfed by those of electrons, positrons, and photons.

After the explosions are launched and the explosion energy approaches to near its saturation level ($t \sim 1.1 - 1.3$ s), we increase the outer boundary of the computational grid, which initially resides within the CO core of the progenitor stars, to a radius of $r = 10^{14}$ cm. Outside of the surface of the progenitors we assume an r^{-2} stellar wind density profile. Enlarging the computational domain allows us to follow the propagation of the SN shock wave through the stars and to simulate large-scale mixing processes during the subsequent evolution until beyond the SN shock breakout from the surface of the progenitors. In these long-time calculations, we neglect neutrino transport and neutrino-matter interactions, and the general-relativistic monopole correction to self-gravity. We switch the EoS table to that of Timmes & Swesty (2000). We refer to Wongwathanarat et al. (2015) for full details of the input physics employed in these calculations. Our 3D long-time simulations of neutrino-driven explosions are stopped at $t \sim 44\,000 - 61\,000$ s.

The pre-SN models described in Sect. 2.1 and 3D simulations of supernova explosions until at least a time close to shock breakout from the star set up the internal problem, which is the explosion mechanism itself.

2.3. Light curves

Our radiation hydrodynamics code Crab (Utrobin 2004, 2007) integrates the spherically symmetric equations. To follow the development beyond our 3D simulations of neutrino-driven explosions, we average the 3D hydrodynamic flow and the distribution of chemical elements on a spherically symmetric grid at specific times and interpolate them onto the computational mass (Lagrangian) grid of the 1D simulations. These data are used as the initial conditions for the external problem of the hydrodynamic modeling of the SN outburst.

The SN explosion is normally initiated by a supersonic piston applied to the bottom of the stellar envelope at the boundary of the $\sim 1.4\,M_\odot$ central core, which is removed from the computational mass domain and assumed to collapse to become a neutron star. With the hydrodynamic flow being given by our 3D simulations of neutrino-driven explosions, we do not need to mimic the explosion by a supersonic piston at the inner boundary and, instead, have to take into account fallback onto the young neutron star, i.e., some portion of the matter outside the neutron star that initially moves out, but eventually falls back. To adequately treat fallback and to estimate its mass, we use a ballistic flow approximation at the inner boundary neglecting pressure effects (e.g., Chevalier 1989). This kind of an inner boundary condition describes the infalling matter or the gas outflowing but bound to the neutron star. The innermost zone, to which this boundary condition is applied, is removed from the numerical mass grid just when its radius reaches a very small value of $0.01\,R_\odot$.

The numerical modeling of the SN outbursts employs the implicit, Lagrangian, radiation hydrodynamics code Crab. The spherically symmetric hydrodynamic equations with a gravity force and radiation transfer equation (e.g., Mihalas & Mihalas 1984) in the one-group (gray) approximation are discretized spatially using the method of lines (e.g., Hairer et al. 1993; Hairer & Wanner 1996). The derived system of ordinary differential equations is stiff and is integrated by the implicit method of Gear (1971) with an automatic choice of both the time integration step and the order of accuracy of the method. To automatically capture shocks, the linear and nonlinear artificial viscosity of Caramana et al. (1998) is added into the hydrodynamic equations. The radiation hydrodynamic equations include additional Compton cooling and heating according to Weymann (1966).

The time-dependent radiative transfer equation, written in a comoving frame of reference to within terms close to the ratio of the matter velocity to the speed of light, is solved as a system of equations for the zeroth and first angular moments of the nonequilibrium radiation intensity. To close this system of moment equations, we use a variable Eddington factor that is calculated by directly taking the scattering of radiation in the ejecta into account. In the inner, optically thick layers of the SN envelope, where thermalization of radiation takes place, the diffusion of equilibrium radiation is described in the approximation of radiative heat conduction. In these layers, local thermodynamic equilibrium (LTE) applies. The bolometric luminosity of the SN is calculated by including retardation and limb-darkening effects. Taking the latter effects into account is necessary to reproduce the bolometric light curve of SN 1987A before and after the broad luminosity peak correctly (Utrobin 2004).

The gamma rays with energies of about 1 MeV from the decay chain $^{56}\mathrm{Ni} \rightarrow {}^{56}\mathrm{Co} \rightarrow {}^{56}\mathrm{Fe}$ deposit their energy through Compton scattering with free and bound electrons. The Compton electrons lose their energy through Coulomb heating of free electrons, and ionization and excitation of atoms and ions. The rates of nonthermal heating, excitation, and ionization of atoms and ions are taken from Kozma & Fransson (1992). They are included in the radiation hydrodynamic equations and the equation of state. The gamma-ray transport is calculated with the approximation of an effective absorption opacity of $0.06\,Y_\mathrm{e}\,\mathrm{cm}^2\,\mathrm{g}^{-1}$. Positrons are assumed to deposit their energy locally.

Generally, the equation of state for an ideal gas in a nonequilibrium radiation field, and for non-thermal excitation and ionization requires solving the problem of the level populations and the ionization balance. The need of corresponding multiple calculations of the equation of state in hydrodynamic modeling forces us to neglect the excited atomic and ionic levels, and to restrict our analysis only to the atomic and ionic ground states, i.e. to their ionization balance. The elements H, He, C, N, O, Ne, Na, Mg, Si, S, Ar, Ca, Fe, and the negative hydrogen ion H^- are included in the non-LTE ionization balance. All elements but H are treated with three ionization stages. The atoms and ions are assumed to consist of the ground state and continuum. The ionization balance is controlled by the following elementary processes: photoionization and radiative recombination, electron ionization and three-particle recombination, and nonthermal ionization. The partition functions are calculated with the polynomial approximation fit obtained by Irwin (1981). The photoionization cross sections of atoms and ions are evaluated with data of Verner & Yakovlev (1995), and Verner et al. (1996). The electron collisional ionization rates for atoms and ions are computed using the approximate formulae of Voronov (1997). The photoionization cross section data for the negative hydrogen ion are taken from Wishart (1979), and the rate coefficient of the electron collisional detachment reaction for the negative hydrogen ion from Janev et al. (1987).

Non-LTE effects are also taken into account when determining the mean opacities, the thermal emission coefficient, and the contribution of lines to the opacity. The mean opacities include processes of photoionization, free-free absorption, Thomson scattering on free electrons, and Rayleigh scattering on neutral hydrogen. The free-free absorption coefficient is calculated with the effective nuclear charge including screening effects (Sutherland & Dopita 1993) and the temperature-averaged free-free Gaunt factor from Sutherland (1998). The free-free absorption coefficient of negative hydrogen ions was calculated by Bell & Berrington (1987). The Rayleigh scattering by hydrogen atoms is calculated using the cross-section of Gavrila (1967) and the exact static dipole polarizability of hydrogen from Teachout & Pack (1971).

The contribution of spectral lines to the opacity in an expanding medium with a velocity gradient is evaluated by the generalized formula of Castor et al. (1975) and is treated as pure scattering. Oscillator strengths of lines are taken from the line database of Kurucz (2002) containing nearly 530 000 lines. Energy level data are from the atomic spectra database of the National Institute of Standards and Technology. Atomic and ionic level populations are determined by the Boltzmann formulae and the Saha equations for a mixture of all elements from H to Zn with the local nonequilibrium radiation temperature.

The main shortcomings of our radiation hydrodynamics code Crab are the assumption of spherical symmetry and the gray approximation for the photon radiation transport. The latter approximation is, however, sufficiently accurate to reproduce the bolometric light curve of SN 1987A. Other codes used in the modeling of supernova light curves are, for example, PHOENIX (see e.g. Hauschildt & Baron 2014) and SEDONA (Kasen et al. 2006), both of which are multidimensional, time-dependent, non-LTE, multi-wavelength radiation transport codes, but no radiation hydrodynamics codes.

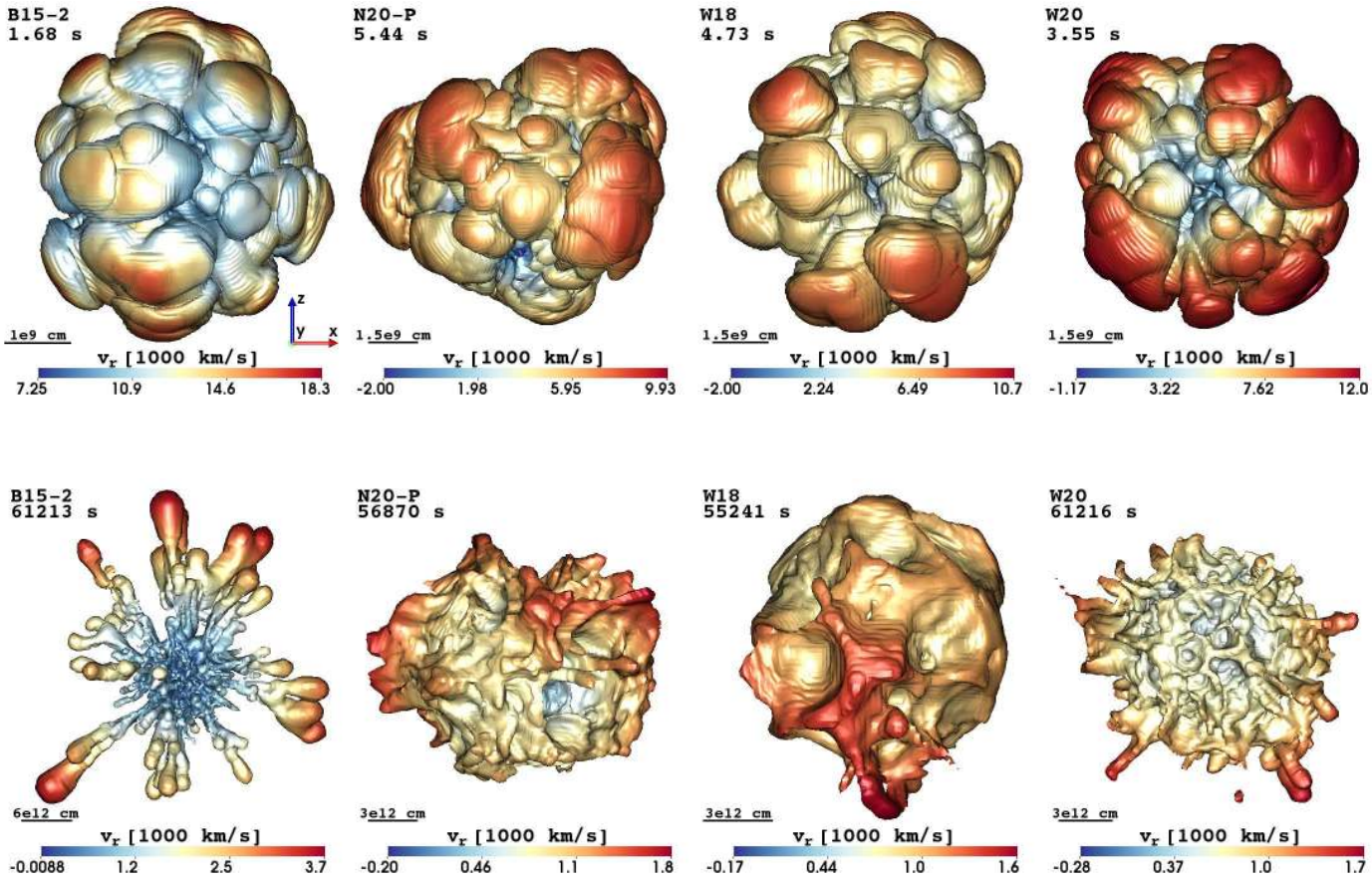

Fig. 3. Morphology of radioactive ^{56}Ni-rich matter produced by explosive burning in shock-heated ejecta. The snapshots display isosurfaces where the mass fraction of ^{56}Ni plus the neutron-rich tracer nucleus equals 3%. The isosurfaces are shown for 3D models B15-2, N20-P, W18, and W20 at two different epochs: shortly before the SN shock crosses the C+O/He composition interface in the progenitor star at $t = 1.68, 5.44, 4.73$, and 3.55 s after bounce (upper row) and long after the shock breakout at $t = 61\,213, 56\,870, 55\,241$, and 61 216 s (lower row), respectively. The colors give the radial velocity on the isosurface, the color coding being defined at the bottom of each panel. In the top left corner of each panel, we give the name of the model and the post-bounce time of the snapshot. The size of the displayed volume and the clumps can be estimated from the yardsticks given in the lower left corner of each panel. One notices a striking difference between model B15-2 and the other models in the final morphology of the ^{56}Ni-rich ejecta, which arises from their specific progenitor structures and the influence of the latter on the unsteady SN shock propagation.

3. Results

A set of 3D neutrino-driven explosion simulations with our four pre-SN models B15, N20, W18, and W20 (Table 1) as initial data is carried out. Basic properties of the averaged 3D simulations for seven computed models are listed in Table 2. We map our 3D simulations to a spherically symmetric grid at two different epochs: at an early time $t^{\rm e}_{\rm map}$, prior to shock breakout, and at a late time $t^{\rm l}_{\rm map}$, long after shock breakout. We use these 1D models mapped from the 3D data as the initial conditions to simulate the SN outburst with the spherically symmetric code Crab. From this point on we will refer to these 1D hydrodynamic models as "early-time or late-time 1D simulations (models)" as a continuation of the corresponding 3D simulations. We define the explosion energy $E_{\rm exp}$ as the sum of the total (i.e., internal plus kinetic plus gravitational) energy of all grid cells at the mapping moment. Throughout this paper, we employ the energy unit 1 bethe = 1 B = 10^{51} erg.

3.1. 3D simulations of the first day of explosion

For completeness we outline the development of neutrino-driven explosions after core bounce (see, e.g., Kifonidis et al. 2003, 2006, for details). As an illustrative example, we consider our reference model B15-2 (see Wongwathanarat et al. 2015, for detailed results and discussion). Neutrino heating around the neutron star triggers violent buoyancy and mass overturn, first visible at about $t = 65$ ms after bounce when Rayleigh-Taylor mushrooms begin to grow from the imposed seed perturbations in the convectively unstable layer that builds up within the neutrino-heating region between the gain radius and the stalled SN shock. These high-entropy bubbles start rising, growing, merging, partially collapsing again, and emerge once more to inflate to larger sizes. Supported by convective overturn and global shock motions, the delayed, neutrino-driven explosion sets in at roughly $t = 164$ ms after bounce.

The value of the explosion energy is determined by the isotropic neutrino luminosity at the inner boundary and its prescribed temporal evolution plus the accretion luminosity, which is regulated by the mass accretion rate of the considered collaps-

Table 2. Basic properties of the averaged 3D simulations.

Model	M_{CC}	M_{env}	E_{exp}	M_{Ni}^{min}	M_{Ni}^{max}	M_{Ni}^{rpr}	t_{map}^{e}	t_{map}^{l}	t_{SB}
	($M_\odot$)		(B)	($10^{-2}\,M_\odot$)			(10^3 s)		
B15-1	1.26	14.19	1.15	2.87	8.25	5.58	6.62	61.2	7.81
B15-2	1.25	14.21	1.40	3.11	9.36	6.23	4.83	61.2	7.10
B15-3	1.25	14.29	2.59	4.81	11.08	7.94	3.99	44.6	5.29
N20-P	1.46	14.72	1.67	4.16	12.11	8.13	3.77	56.9	5.36
N20-C	1.46	14.72	1.67	4.16	12.11	8.13	3.71	56.9	5.35
W18	1.40	15.52	1.36	3.67	12.97	8.32	3.40	55.2	4.26
W20	1.50	17.92	1.45	4.10	13.04	8.57	4.21	61.2	6.67

Notes. The computed models are based on the corresponding pre-SN models of Table 1, except for model N20-C, which has the same composition of metals as model N20-P with its hydrogen mass fraction enhanced to $X_{surf} = 0.735$ at the expense of helium in the hydrogen-rich envelope. M_{CC} is the mass of the collapsing core; M_{env}, the ejecta mass; E_{exp}, the explosion energy; M_{Ni}^{min}, the mass of radioactive ^{56}Ni produced directly in shock-heated ejecta by our reaction network; M_{Ni}^{max}, the aggregate mass of directly produced ^{56}Ni and tracer nucleus; and M_{Ni}^{rpr}, the representative radioactive ^{56}Ni mass containing the whole directly produced ^{56}Ni and half of the tracer nucleus. t_{map}^{e} and t_{map}^{l} are the two moments at which the 3D simulations are mapped to a spherically symmetric grid. t_{SB} is the epoch of shock breakout in the early-time 1D simulations.

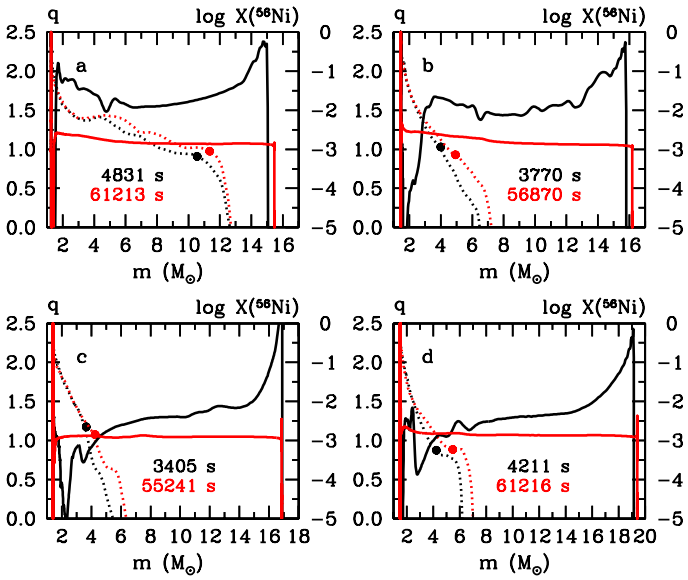

Fig. 4. The approach to homologous expansion is shown by comparing the early-time (*black lines*) and late-time (*red lines*) 3D simulations of models B15-2 (Panel **a**), N20-P (Panel **b**), W18 (Panel **c**), and W20 (Panel **d**). The *solid lines* give the homology index $q = \partial \ln v / \partial \ln r$, the *dotted lines* the ^{56}Ni mass fraction. *Bullets* mark the outer boundary of the bulk of ^{56}Ni containing 99% of the total ^{56}Ni mass.

ing stellar core and by the gravitational potential of the accreting neutron star, which depends on the contraction of the inner boundary.

Once the shock wave has been launched by neutrino heating, the further evolution of the explosion depends strongly on the density profile of the pre-SN. It is known that the shock decelerates whenever it encounters a density profile that falls off with increasing value ρr^3, while it accelerates for density profiles with decreasing value ρr^3. Since the density structure of pre-SN models cannot be described by a single power law (Figs. 1b and d), the shock propagates nonmonotonically. At the locations of the Si/O, (C+O)/He, and He/H interfaces (Fig. 2), the radial dependence of the value of ρr^3 varies, i.e., the velocity of the shock increases when the shock approaches a composition interface and decreases after the shock has crossed the interface.

The shock wave first reaches the Si/O interface at around $t = 252$ ms after bounce. When it crosses the (C+O)/He interface at $t = 1.68$ s after bounce, the maximum speed of the ^{56}Ni-rich matter is as high as $\approx 18\,300$ km s^{-1} (Fig. 3, left panel in upper row). Thereafter, a rapid decrease of the shock velocity occurs when the shock enters the He-layer, and a reverse shock forms at around $t = 15$ s after core bounce. Once the main shock has passed the He/H interface around $t = 66$ s after bounce, the evolution resembles that after the crossing of the (C+O)/He interface and another reverse shock forms below the He/H interface at around $t = 700$ s. A few of the fastest Rayleigh-Taylor plumes have actually reached the He/H interface before this strong reverse shock has formed, and thereby they have escaped an interaction with this shock in stark contrast to the situation in the other models N20-P, W18, and W20 (Fig. 3). The motion of the fastest metal clumps relative to the background flow never becomes supersonic, and the deceleration enhanced by supersonic drag is absent. Hence, the maximum velocities of iron-group nuclei and other elements decrease only slightly at late times, and the fastest ^{56}Ni-rich clumps move with velocities of ≈ 3700 km s^{-1} at $t = 61\,213$ s after bounce (Fig. 3, first panel in lower row). In contrast, the other mushrooms penetrate through the reverse shock and move supersonically relative to the ambient medium. As a result they dissipate a large fraction of their kinetic energy in bow shocks and strong acoustic waves, and form an almost spherical distribution with velocities up to ≈ 1000 km s^{-1} by $t = 61\,213$ s after bounce.

An unsteady shock propagation through the pre-SN gives rise to Rayleigh-Taylor unstable (opposite) pressure and density gradients at the composition interfaces. A global deformation of the main shock enhances strong inward mixing of hydrogen: the aspherical shock deposits large amounts of vorticity into the He/H interface layer and triggers the growth of a strong Richtmyer-Meshkov instability. The latter creates huge hydrogen pockets at the He/H interface intensifying mixing of hydrogen-rich matter down to the center. It should be emphasized that this instability plays a less important role in the 3D simulations of Hammer et al. (2010) and Wongwathanarat et al. (2015) than in the 2D models of Kifonidis et al. (2003, 2006). The 3D dynamics of outward mixing of radioactive ^{56}Ni and inward mixing of hydrogen-rich matter in the SN models was studied in detail by Wongwathanarat et al. (2015).

During the propagation of the main shock before its breakout, the shock deformation is imprinted on the ejecta and determines the morphology of the outer layers. To measure the asphericity of the outer layers in the late-time 3D simulations of models B15-2, N20-P, W18, and W20, we approximated the density isosurface with an ellipsoid in the vicinity of the photosphere position found for the averaged 3D simulations. The maximum ratios of the semiaxes for the approximations thus obtained are 1.055, 1.058, 1.030, and 1.025, respectively.

3.2. Approach to homologous expansion

As pointed out above, there is observational evidence for macroscopic mixing occurring during the explosion of SN 1987A. Mixing of radioactive ^{56}Ni out of the center and hydrogen-rich matter down to the center is required in order to reproduce both

the smooth rising part of the bolometric light curve and the width of the broad maximum. Because macroscopic mixing continues until a phase when the ejecta reach a homologous expansion, we are interested in carrying out our 3D simulations of SN explosions as long as possible. Homologous expansion occurs when the contribution of pressure and gravity to the momentum equation may be neglected. A convenient measure to control the approach of the hydrodynamic flow to homologous expansion is the effective homology index $q = \partial \ln v / \partial \ln r$, which has to go to unity.

We estimate the proximity to homologous expansion by comparing the averaged 3D simulations at the two different mapping epochs (Table 2, Fig. 4). At the early-time mapping epoch, $t^{\rm e}_{\rm map}$, well prior to the phase of shock breakout, the hydrodynamic flow is far from homologous expansion in all four models B15-2, N20-P, W18, and W20 because the index q varies over a wide range around unity. It implies that outward mixing of radioactive ^{56}Ni and inward mixing of hydrogen-rich matter in the ejecta will continue until complete homology is reached. By the late-time mapping epoch, $t^{\rm l}_{\rm map}$, the index q is very close to unity in all models, and the ejecta in the 3D neutrino-driven simulations of these models are almost in homologous expansion. It is clear that between $t^{\rm e}_{\rm map}$ and $t^{\rm l}_{\rm map}$ macroscopic mixing of radioactive ^{56}Ni will continue (Fig. 4). For this reason, the 3D neutrino-driven simulations mapped at the early-time epoch are less reliable than those evolved to the late-time mapping epoch. At $t^{\rm l}_{\rm map}$ the index q is closer to unity in the outer layers of the ejecta than in the inner layers because the contribution of pressure and gravity to the momentum equation is smaller in the outer layers than in the inner layers. At $t^{\rm l}_{\rm map}$ the bulk of ^{56}Ni containing 99% of the total ^{56}Ni mass expands almost homologously in all four models (Fig. 4).

However, to predict the subsequent evolution of the nickel ejecta, one would have to take additional mixing into account that might result from local radioactive decay heating (see also Sect. 4). Herant & Benz (1991) performed 2D simulations of hydrodynamic instabilities and mixing in SN 1987A during the period from 400 min to 90 days. They showed that ^{56}Ni and subsequent ^{56}Co decay leads to a relatively modest boost of the peak radial velocities of these elements by a few hundred km s^{-1}. Because of this relatively small change in the velocities of iron-group elements by radioactive decay heating, we consider our 3D models mapped at $t^{\rm l}_{\rm map}$ as a good proxy of the final state with respect to mixing and velocity distributions of heavy elements. After mapping the peak radial velocity of the ^{56}Ni-rich matter increases by radioactive decay heating, which is treated adequately in the Crab code.

We first analyze the hydrodynamic flow, which is characterized, among other factors, by the velocity profile. In the homologous expansion phase, the expansion velocity of the outermost layers in models B15-2, N20-P, W18, and W20 exceeds a value of $\approx$36 000 km s^{-1} for the early-time 1D simulations (Fig. 5). This is consistent with observations of the radio remnant of SN 1987A over the period from 1987 to 1990–1991, implying a mean expansion speed of $\approx$38 000 km s^{-1} (Gaensler et al. 2007). At the same time, the late-time 1D models result in an expansion velocity of the outermost layers that is a factor of three lower than that for the early-time 1D models (Fig. 5).

This disagreement between the early- and late-time runs is a numerical artifact that originates from the interaction of the shock with an assumed stellar wind, surrounding the pre-SN model. For the Eulerian simulations with the Prometheus code, an ambient medium (e.g., in the form of a stellar wind) is necessary to follow the 3D neutrino-driven simulations after the shock breakout, while this assumption is not needed for the Lagrangian simulations with the Crab code. It turns out that the chosen stellar wind is too dense to reproduce the shock velocities after breakout correctly. Unfortunately, because of the computational cost of 3D simulations, we are not able to iterate the stellar wind parameters to minimize the influence of the wind on the velocity of the outermost layers after shock breakout. Generally speaking, there is no reason to make efforts to eliminate this artifact because even in the case of the early-time 1D runs the light curve is inconsistent with the observations of SN 1987A during the first 30 days (see, for example, for model B15-2 in Fig. 6a).

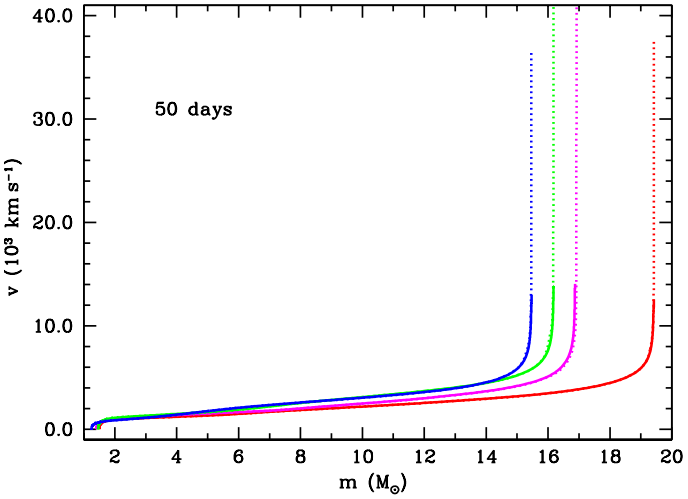

Fig. 5. Velocity of the ejecta as function of interior mass in models B15-2 (*blue line*), N20-P (*green line*), W18 (*magenta line*), and W20 (*red line*) at t = 50 days for the early-time (*dotted lines*) and late-time (*solid lines*) 1D simulations.

We now address the mixing of radioactive ^{56}Ni and hydrogen during the explosion and the light curve properties for the early- and late-time 1D simulations of model B15-2. Figure 6c shows the mass fractions of hydrogen, helium, CNO group elements, and iron group elements as functions of velocity for the early-time 1D simulations. Between $t^{\rm e}_{\rm map}$ and $t^{\rm l}_{\rm map}$, macroscopic mixing in the ejecta increases both the mass fraction of hydrogen in the metal core (Fig. 6b) and that of radioactive ^{56}Ni in the outer part of the mixing zone, with the maximum ^{56}Ni velocity remaining unchanged (Fig. 6d). These changes may be considered as insignificant compared to the dramatic evolution of the hydrodynamic flow during that period (Fig. 4). In addition, this result justifies a terminal time for 3D simulations of the order of 55 000 – 60 000 s after bounce.

A redistribution of radioactive ^{56}Ni to higher velocities in the mixing zone slightly increases the bolometric luminosity relative to the early-time 1D run between ~30 days and ~60 days (Fig. 6a), at which time the radioactive decay of ^{56}Ni and ^{56}Co nuclides becomes dominant in powering the luminosity. An increase of the mass fraction of hydrogen in the metal core enlarges the opacity and the optical depth of the inner part of the ejecta and, consequently, the photon diffusion time, making the dome-like maximum of the light curve slightly lower and wider (Fig. 6a). Both effects tend to improve the match between computed and observed light curves, and therefore we focus mainly on hydrodynamic models for the late-time 1D simulations.

In the radioactive tail the same (to an accuracy of 0.5%) total ^{56}Ni mass results in a luminosity that is higher by $\approx$3% compared to the early-time 1D models (Fig. 6a). This behavior of the lu-

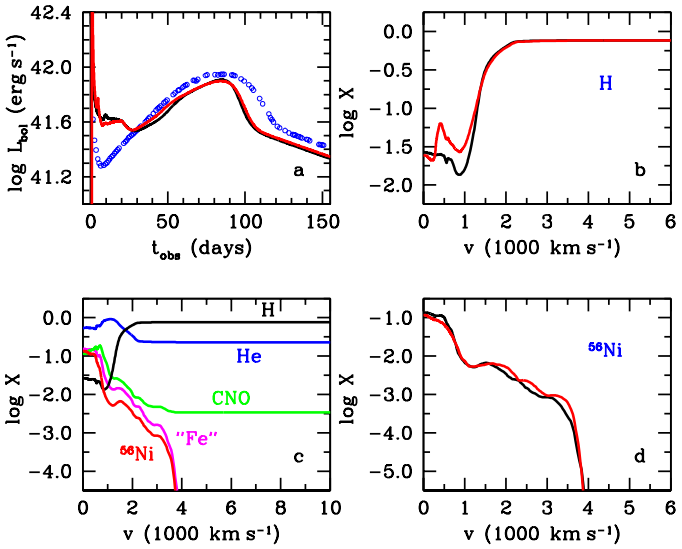

Fig. 6. Comparison of the early- and late-time 1D simulations for model B15-2 with the representative radioactive ^{56}Ni mass (Table 2). Panel **a**: bolometric light curves of the early-time (*black line*) and late-time (*red line*) 1D simulations compared with the observations of SN 1987A obtained by Catchpole et al. (1987, 1988) (*open circles*). Panels **b** and **d**: mass fractions of hydrogen and radioactive ^{56}Ni, respectively, as functions of velocity for the early-time (*black line*) and late-time (*red line*) 1D simulations. Panel **c**: mass fractions as functions of velocity for the early-time 1D simulation. The *red line* is the mass fraction of radioactive ^{56}Ni (see also Fig. 2). All profiles of the mass fractions are given at $t = 50$ days.

minosities is caused by the difference in the expansion velocities of the outermost layers for the early and late-time 1D simulations (Fig. 5). The higher velocities of the outermost layers for the early-time 1D simulations imply a higher rate of work done by radiation pressure. Utrobin (2007) showed that the higher the rate of work done by radiation pressure is in a SN envelope, the larger is the excess of the gamma-ray luminosity (for a given total ^{56}Ni mass) over the bolometric luminosity in the radioactive tail when the SN envelope still remains optically thick for gamma rays.

3.3. Mixing of radioactive ^{56}Ni and hydrogen

Along with the explosion energy and the total amount of radioactive ^{56}Ni (Table 2), our 3D supernova simulations can be characterized by the macroscopic mixing of ^{56}Ni and hydrogen-rich matter occurring during the SN explosion. In Table 3 we summarize some global properties of the mixing induced by the 3D neutrino-driven explosions in the ejecta at $t^{1}_{\rm map}$, assuming that the bulk mass of ^{56}Ni contains 99% of the total ^{56}Ni mass and the fast moving ^{56}Ni tail contains the remaining 1%. Dividing the total amount of radioactive ^{56}Ni into a slow moving bulk and a fast moving tail is motivated by the evidence for a fast ^{56}Ni clump of $\sim 10^{-3}\,M_\odot$ observed in SN 1987A (Utrobin et al. 1995), which can be identified with what we define as tail. Mixing of hydrogen-rich matter may be measured by the mass of hydrogen mixed into the He shell or even better by the average mass fraction of hydrogen $\langle X\rangle$ in the mass shell defined by $M_{\rm CC} \leqq m(r) \leqq \min(M^{\rm core}_{\rm He}, M_{\rm mix})$, where $M_{\rm CC}$ and $M^{\rm core}_{\rm He}$ are the mass coordinates of the outer edge of the collapsing core and the helium core (Tables 2 and 1), respectively.

Table 3. Some global properties of mixing in the ejecta.

Model	$\langle v\rangle^{\rm bulk}_{\rm Ni}$	$v^{\rm bulk}_{\rm Ni}$	$\langle v\rangle^{\rm tail}_{\rm Ni}$	$M_{\rm mix}$	$\delta M_{\rm H}$	$\langle X\rangle$
	($\rm km\,s^{-1}$)			($M_\odot$)		
B15-1	921	3103	3241	11.45	0.111	0.040
B15-2	1222	3355	3490	11.20	0.172	0.062
B15-3	1807	4977	5678	12.31	0.329	0.118
N20-P	924	1635	1790	4.80	0.262	0.039
N20-C	930	1642	1797	4.79	0.375	0.052
W18	877	1395	1472	4.10	0.062	0.011
W20	783	1374	1482	5.32	0.083	0.012

Notes. The left column gives the name of the hydrodynamic model. $\langle v\rangle^{\rm bulk}_{\rm Ni}$ is the weighted mean velocity of the bulk mass of ^{56}Ni with the ^{56}Ni mass fraction as weight function; $v^{\rm bulk}_{\rm Ni}$, the maximum velocity of the bulk mass of ^{56}Ni; $\langle v\rangle^{\rm tail}_{\rm Ni}$, the weighted mean velocity of the fast moving ^{56}Ni tail with the ^{56}Ni mass fraction as weight function; $M_{\rm mix}$, the mass coordinate out to which the bulk mass of ^{56}Ni is mixed; $\delta M_{\rm H}$, the mass of hydrogen mixed into the He shell; and $\langle X\rangle$ is the average mass fraction of hydrogen in the mass shell defined by $M_{\rm CC} \leqq m(r) \leqq \min(M^{\rm core}_{\rm He}, M_{\rm mix})$, where $M_{\rm CC}$ and $M^{\rm core}_{\rm He}$ are the mass coordinates given in Tables 2 and 1, respectively.

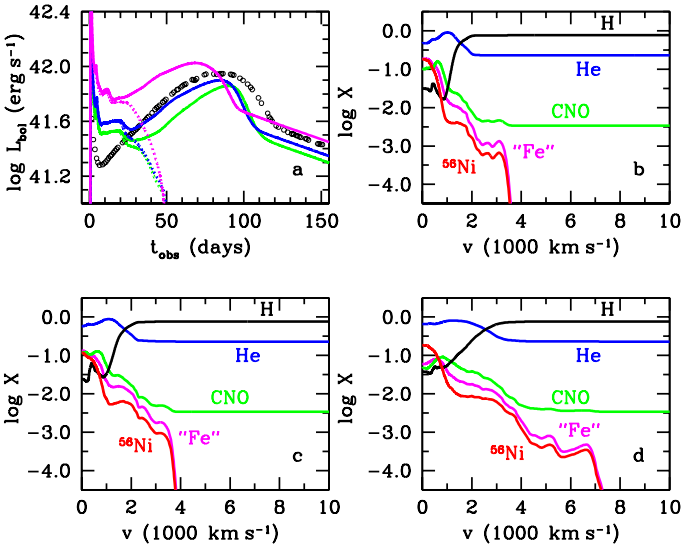

Fig. 7. Dependence of the bolometric light curve and the mass fractions at $t = 50$ days on the explosion energy for the late-time 1D simulations with the representative radioactive ^{56}Ni mass from Table 2. Panel **a** shows the light curves of models B15-1 (*green solid line*), B15-2 (*blue solid line*), and B15-3 (*magenta solid line*) compared with the observations of SN 1987A obtained by Catchpole et al. (1987, 1988) (*open circles*). The light curves of the corresponding models without radioactive ^{56}Ni are shown with dotted lines. Panels **b**, **c**, and **d** show the mass fractions as functions of velocity in models B15-1, B15-2, and B15-3, respectively. The *red line* is the mass fraction of radioactive ^{56}Ni, and the *magenta line* represents iron-group elements except for ^{56}Ni (see also Fig. 2).

Models B15-1, B15-2, and B15-3 show that the production of radioactive ^{56}Ni is proportional to the explosion energy (Table 2). At the same time, the production of radioactive ^{56}Ni reveals no clear dependence on pre-SN properties, if neutrino-driven SN explosion models with similar explosion energies are compared. The pre-SN models B15, N20, W18, and W20 have different helium cores in the mass range from 4 to 7.5 $M_\odot$ (Table 1), different density structures (Fig. 1), different compact-

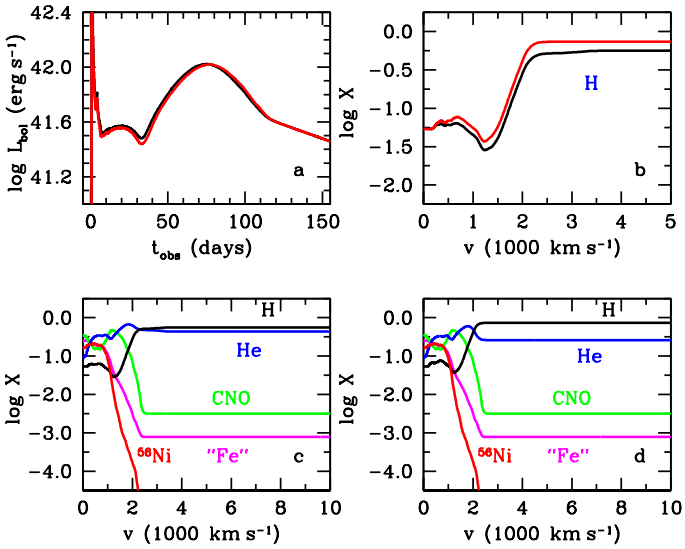

Fig. 8. Dependence of the bolometric light curve and the hydrogen mixing on the chemical composition of the hydrogen-rich envelope for the late-time 1D N20 models with the representative radioactive ^{56}Ni mass from Table 2. Panel **a** shows the bolometric light curves of models N20-P (*black line*) and N20-C (*red line*). Panel **b** shows the mass fraction of hydrogen as function of velocity in models N20-P (*black line*) and N20-C (*red line*). Panels **c** and **d** give the mass fractions as functions of velocity in models N20-P and N20-C, respectively. The *red line* is the mass fraction of radioactive ^{56}Ni, and the *magenta line* represents iron-group elements except for ^{56}Ni (see also Fig. 2). All profiles of the mass fractions are given at $t = 50$ days.

ness values $\xi_{1.5}$ for 1.5 $M_\odot$ enclosed mass (Table 1), and different chemical compositions (Fig. 2). A sequence of models B15-2, N20-P, W18, and W20 with comparable explosion energies reveals no clear correlation between the production of radioactive ^{56}Ni and these pre-SN properties, although an increasing trend can be noticed in this sequence of models with nearly the same explosion energy.

Models B15-1, B15-2, and B15-3 demonstrate that the greater the explosion energy (Table 2), the more intense is the mixing of radioactive ^{56}Ni in velocity space (Table 3, Figs. 7b-d), the greater is the average mass fraction of hydrogen $\langle X \rangle$, and the higher is the mass of hydrogen mixed into the He shell (Table 3). The variety of pre-SN properties provides an opportunity to study the sensitivity of the outward ^{56}Ni mixing and the inward hydrogen mixing to the structure of the helium core and the He/H composition interface, a connection that was discovered by Kifonidis et al. (2006) and further studied by Wongwathanarat et al. (2015). It turns out that in the sequence of models B15-2, N20-P, W18, and W20 with comparable explosion energies (Table 3), the mixing of radioactive ^{56}Ni in velocity space and the average mass fraction of hydrogen $\langle X \rangle$ decrease, while the mass of hydrogen mixed into the He shell does not show any correlation. There is no leading single parameter that explains this finding, because the large-scale mixing is the result of a complex sequence of progenitor-structure dependent hydrodynamic instabilities at the composition interfaces (cf. Wongwathanarat et al. 2015). It is noteworthy that in all hydrodynamic models the minimum velocity of hydrogen-rich matter is less than 100 km s^{-1}.

From about day 7 to day 30 the bolometric light curve is mainly determined by the properties of a cooling and recombination wave (CRW). In the context of SN 1987A, a basic CRW property reads that the higher the ratio of the explosion energy to the ejecta mass, the higher the luminosity in the CRW phase because the ejecta expand and cool more quickly (Woosley 1988; Utrobin 1989; Shigeyama & Nomoto 1990). This dependence is distinctly demonstrated by the sequence of models B15-1, B15-2, and B15-3 (Table 2, Fig. 7a). After the CRW stage, when the radiative diffusion takes place, the radioactive decay of ^{56}Ni and ^{56}Co nuclides becomes dominant in powering the luminosity. It is evident that in this period the bolometric light curve depends on the amount of radioactive material and its distribution over the ejecta.

Table 4. Radioactive ^{56}Ni masses from fit to observations.

Model	M_i^e	M_i^l	M_f^e	M_f^l	δM_{Ni}^e	δM_{Ni}^l	δM_{tot}^e	δM_{tot}^l
	(10^{-2} $M_\odot$)					(10^{-4} $M_\odot$)		
B15-1	7.52	7.29	7.42	7.26	9.2	2.4	33.2	10.2
B15-2	7.52	7.29	7.47	7.28	4.5	0.9	24.8	6.7
B15-3	7.73	7.37	7.72	7.37	1.8	0.5	6.7	2.8
N20-P	7.69	7.26	7.55	7.23	14.1	2.5	97.2	21.0
N20-C	7.69	7.26	7.55	7.23	14.1	2.5	96.4	20.1
W18	8.53	7.33	7.68	7.26	84.8	7.2	417.3	60.8
W20	7.87	7.31	7.46	7.24	40.5	7.1	107.7	39.6

Notes. The names of the hydrodynamic models are given in the left column. M_i^e and M_i^l are the initial ^{56}Ni masses computed at the onset of light curve modeling t_{map}^e and t_{map}^l, respectively (see Table 2). The other columns provide the ^{56}Ni mass ejected at day 150, M_f, the fallback mass of ^{56}Ni, δM_{Ni}, during the period from t_{map} to day 150, and the total fallback mass, δM_{tot}, during the same period; all values for the early- and late-time 1D simulations. Note that $M_f = M_i - \delta M_{Ni}$.

Finally, we study the influence of the chemical composition of the hydrogen-rich envelope on the mixing of radioactive ^{56}Ni and hydrogen. For this purpose, we construct an additional model, N20-C, which has the same metal composition as model N20-P, except the hydrogen mass fraction is enhanced to $X_{surf} = 0.735$ at the expense of helium in the hydrogen-rich envelope (Tables 1 and 2). The increase of the hydrogen abundance from that of the original pre-SN model N20-P to the one of model N20-C turns out not to affect the production of radioactive ^{56}Ni and its mixing (Table 3, Figs. 8c and d). It only slightly increases the hydrogen mass fraction in the mixing zone (Table 3, Fig. 8b). As a result, the mass fraction of hydrogen in model N20-C exceeds that in model N20-P throughout the ejecta.

Another CRW property states that the higher the mass fraction of hydrogen is and the lower the mass fraction of helium, the lower is the effective temperature in the CRW phase (Grassberg & Nadyozhin 1976; Utrobin 1989). For a constant explosion energy, this statement may be reformulated for the luminosity in the CRW phase: the higher the mass fraction of hydrogen and the lower the mass fraction of helium are, the lower the luminosity. This is confirmed by the light curves of models N20-P and N20-C for the period from day 7 to day 33 (Fig. 8a). A small increase of the mass fraction of hydrogen in the mixing zone makes the innermost layers of the ejecta more opaque and, as a consequence, increases the diffusion time and slightly shifts the dome-like maximum of the light curve of model N20-C as a whole to later times relative to that of model N20-P (Fig. 8a).

3.4. Comparison with observations

A comparison of the calculated light curves of models B15-1, B15-2, and B15-3 (Table 2) with the observed light curve

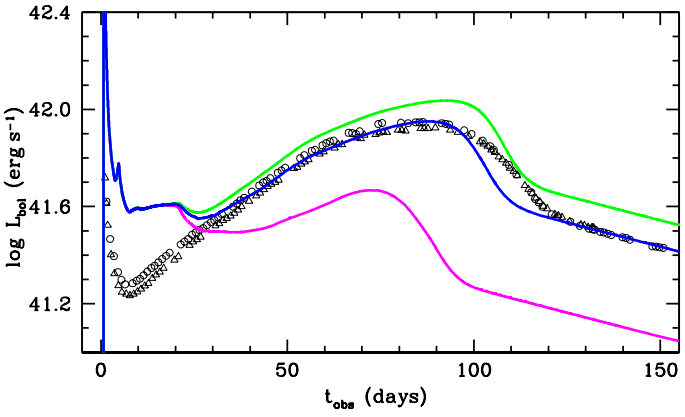

Fig. 9. Bolometric light curves of model B15-2 with the mass scaled to fit the observed luminosity in the radioactive tail, $M_{\rm f}^{\rm l}$ (see Table 4) (*blue line*), the mass of radioactive ^{56}Ni produced directly by our reaction network, $M_{\rm Ni}^{\rm min}$ (*magenta line*), and the aggregate mass of directly produced ^{56}Ni and tracer nucleus, $M_{\rm Ni}^{\rm max}$ (*green line*), (see Table 2) for the late-time 1D simulations compared with the observations of SN 1987A obtained by Catchpole et al. (1987, 1988) (*open circles*) and Hamuy et al. (1988) (*open triangles*).

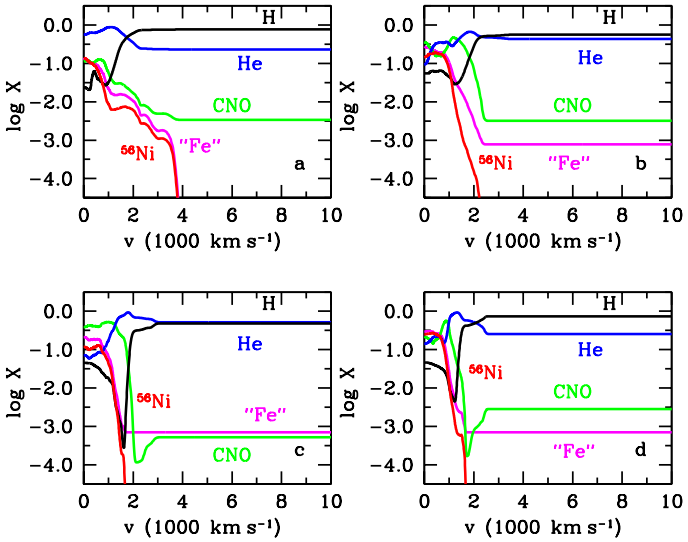

Fig. 10. Mass fractions of hydrogen (*black line*), helium (*blue line*), CNO group elements (*green line*), iron group elements except for ^{56}Ni (*magenta line*), and radioactive ^{56}Ni (*red line*) as functions of velocity at day 50 in models B15-2 (Panel **a**), N20-P (Panel **b**), W18 (Panel **c**), and W20 (Panel **d**) for the late-time 1D simulations. In all models the total ^{56}Ni mass is scaled to fit the observed luminosity in the radioactive tail (see Table 4 and Fig. 11).

(Fig. 7a) shows that an explosion energy of 1.4 B seems to be close to the optimal value for the given pre-SN model. These light curves were computed with the representative ^{56}Ni masses from Table 2, which are a measure of the ^{56}Ni production during the 3D neutrino-driven explosion. It is obvious that these representative ^{56}Ni masses fail to perfectly reproduce the observed luminosity in the radioactive tail of SN 1987A (Fig. 7a).

To match the observations in the radioactive tail, we adjusted the ejected mass of ^{56}Ni, taking the fallback of radioactive ^{56}Ni after the onset of the light curve modeling (Table 4) into account. Figure 9 shows the corresponding light curve for model B15-2 with the adjusted ^{56}Ni mass. In addition, the dependence of the light curve of this model on the ^{56}Ni mass and its distribution is demonstrated by the exemplary models with minimum, $M_{\rm Ni}^{\rm min}$, and maximum, $M_{\rm Ni}^{\rm max}$, nickel masses (see Table 2). The uncertainty in the absolute yield of ^{56}Ni comes, as mentioned above, from our small nuclear network and the approximate neutrino transport. The light curves of the exemplary models reliably comprise the observed luminosity in the radioactive tail (Fig. 9). Maximum velocities of the bulk of ejected ^{56}Ni in the models with the minimum and maximum ^{56}Ni masses differ by less than 100 km s^{-1}. This difference is too small to change the luminosity noticeably at the end of the CRW stage. Subsequently, the light curves are completely determined by the total ^{56}Ni mass (Fig. 9).

For models B15-2, N20-P, W18, and W20 the resultant mass fraction profiles are shown in Fig. 10, and the fit to the observations in the radioactive tail is illustrated by Fig. 11. Because of a different rate of work done by radiation pressure (see Sect. 3.2) and a different fallback of radioactive ^{56}Ni for the early- and late-time 1D simulations, our estimate of the required amount of ^{56}Ni differs for both runs. The initial ^{56}Ni masses for the early- and late-time 1D simulations (Table 4) fall in between the minimum, $M_{\rm Ni}^{\rm min}$, and maximum, $M_{\rm Ni}^{\rm max}$, values (Table 2). Thus, all 3D neutrino-driven simulations under study are able to synthesize the required amount of ejected radioactive ^{56}Ni. Note that the fallback of radioactive ^{56}Ni is not negligible, especially in the case of the early-time 1D simulations.

The total mass of radioactive ^{56}Ni may be evaluated by equating the observed bolometric luminosity in the radioactive tail to the gamma-ray luminosity. We call this mass the observed amount of radioactive ^{56}Ni. This procedure for SN 1987A gives a mass of 0.0722 $M_\odot$. As expected, all ejected masses of ^{56}Ni listed in Table 4 exceed this value because of the discussed expansion-work effects. For the early-time 1D simulations, which produce the correct hydrodynamic flow in the outermost layers (Fig. 5), these differences are on average roughly 5%. We emphasize that the observed amount of radioactive ^{56}Ni should be distinguished from the ejected amount because using the former results in an underestimate of the total ^{56}Ni mass.

An analysis of SN 1987A observations revealed the fact that radioactive ^{56}Ni was mixed in the ejecta up to a velocity of about 3000 km s^{-1}. Only models B15-1 and B15-2 yield the maximum velocity of the bulk mass of ^{56}Ni consistent with the observations, with ^{56}Ni being concentrated around a velocity of $\sim$1000 km s^{-1} (Table 3, Figs. 7b and c). Model B15-3 with an explosion energy of 2.59 B produces mixing that is too strong, while models N20-P, N20-C, W18, and W20 with SN 1987A-like explosion energies, in turn, yield insufficient mixing. This weak mixing of ^{56}Ni in the ejecta of models N20-P, W18, and W20 slows down the outward diffusion of gamma-rays, admitting a decrease in the luminosity after the CRW phase similar to the case of models without radioactive ^{56}Ni (compare Figs. 7a and 11). When the diffusion of gamma-rays becomes efficient, the wide and deep dip of the bolometric light curve at around 30 – 40 days turns into a luminosity rise to maximum (Fig. 11).

The existence of a fast ^{56}Ni clump with an absolute velocity of $\approx$4700 km s^{-1} and a mass of $\sim 10^{-3}$ $M_\odot$ in the SN 1987A envelope (Utrobin et al. 1995) is an important observational fact that should be explained in the framework of neutrino-driven explosions. The development of clumps is successfully reproduced in 3D neutrino-driven simulations as is apparent, for example, from the first panel in the bottom row of Fig. 3. The characteristic velocities of the ^{56}Ni tail, which we have introduced to analyze the generated ^{56}Ni-rich clumps as listed in Table 3, however, fall short of the maximum velocities of clumps in SN 1987A. The

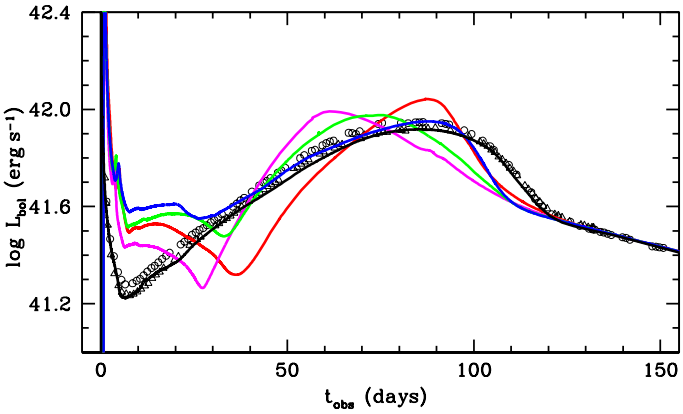

Fig. 11. Bolometric light curves of models B15-2 (*blue line*), N20-P (*green line*), W18 (*magenta line*), and W20 (*red line*) for the late-time 1D simulations compared with the observations of SN 1987A obtained by Catchpole et al. (1987, 1988) (*open circles*) and Hamuy et al. (1988) (*open triangles*). In all models the total ^{56}Ni mass is scaled to fit the observed luminosity in the radioactive tail (see Table 4). In contrast, the *black line* shows the bolometric light curve of an optimal model with a nonevolutionary pre-SN (Utrobin 2005, see also Fig. 1).

only exception is the high-energy model B15-3, whose mean velocity of the ^{56}Ni tail is consistent with the absolute velocity of the fast ^{56}Ni clump in SN 1987A.

Observational evidence for the existence of hydrogen-rich matter within the core of heavy elements of SN 1987A implies a deep macroscopic mixing down to a velocity of $\sim$500 km s^{-1}. It is remarkable that in all models hydrogen mixing occurring during the 3D neutrino-driven simulations results in minimum velocities of hydrogen-rich matter of less than 100 km s^{-1} (Figs. 7b, c, and d; 8c and d; 10). This is in good agreement with the spectral observations.

A very disappointing result is that the calculated light curves of all models B15-2, N20-P, W18, and W20 roughly having the SN 1987A explosion energy are inconsistent with the observations of SN 1987A during the first 30 – 40 days (Fig. 11). First, in all considered models the initial luminosity peak of the light curve is considerably wider than that observed. This indicates that an adequate configuration of the pre-SN has to be more compact. Second, the calculated light curves of all selected models fail to develop a prominent minimum as it is observed at around day 8. Models without radioactive ^{56}Ni (Fig. 7a, dotted lines) show that this discrepancy is caused by the structure of the outer layers of the pre-SN models (Table 1, Fig. 1). Thus, the structure of the outer layers of the available pre-SN models does not agree with that of the BSG Sanduleak $-69^{\circ}202$ just prior to the explosion.

In the sequence of models B15-2, N20-P, and W20 all characteristic velocities describing mixing of radioactive ^{56}Ni decrease (Table 3) and are inversely related to the times of the distinct local minimum of the light curve at which the luminosity starts to grow to the maximum (Fig. 11). The higher the characteristic velocity of ^{56}Ni mixing, the earlier the start of the growth of the luminosity to the maximum. Model W18 differs in this respect because of its low luminosity in the CRW phase, which is caused by the lower density in the outer layers of the corresponding pre-SN model compared to the other models (Fig. 1b). The local minimum of the light curve of model B15-2 is more shallow compared to those of models N20-P, W18, and W20. This reflects the fact that the photosphere enters the mixing zone containing the bulk of ^{56}Ni before the CRW phase ends and, as a consequence, the luminosity does not fall off significantly. In the models N20-P, W18, and W20, the characteristic velocities of ^{56}Ni mixing are so low that a transition from the CRW phase to the stage of exhaustion of stored radiation energy occurs earlier than the photosphere enters the mixing zone. As a result, we see deeper local minima of the light curves (Fig. 11). This situation permits us to describe photon diffusion from the mixing zone to the photosphere using a simple one-zone approximation (Arnett 1979). We estimated the characteristic diffusion times just after the local minimum following the CRW phase and found that these times are consistent, with an accuracy of $\sim$35%, with the characteristic times of the luminosity growth at the same epochs. For models N20-P, W18, and W20 these times of the luminosity growth are about 19, 15, and 19 days, respectively.

As noted earlier, the broad maximum of the light curve is entirely powered by the ^{56}Ni$\rightarrow^{56}$Co$\rightarrow^{56}$Fe decay. The total amount of radioactive ^{56}Ni is measured by the SN luminosity in the radioactive tail, while its mixing throughout the ejecta affects the opacity of the inner layers to which hydrogen makes a major contribution. The density profile, chemical composition, and opacity of these layers determine the optical depth and, consequently, the characteristic diffusion time. The shape of the bolometric light curve near the maximum, in turn, depends on this diffusion time. The characteristic mass fraction of hydrogen $\langle X\rangle$ of models W18 and W20 is about 0.01 (Table 3), which results in a peak-like shape of the light curve maximum. In contrast, the characteristic mass fraction in models B15-2 and N20-P is nearly 0.04 – 0.06, which leads to a longer diffusion time and a dome-like shape (Fig. 11).

It is evident that the dome of the light curve of model B15-2 for the late-time 1D simulations agrees with the observations of SN 1987A much better than that of the other models (Fig. 11). A deficit of the luminosity during the transition from the maximum to the radioactive tail, between roughly day 100 and day 120, is the only defect in the dome shape. This luminosity deficit is equivalent to a deficit in the radiated energy. We have explored the sensitivity of this deficit to different factors and found that only an increase of the ejecta mass with a proportional increase of the explosion energy (to keep the ratio of ejecta mass to explosion energy constant) is able to eliminate this kind of deficit of the luminosity after the main maximum. The explanation is simple: a higher ejecta mass favors an increase of both the stored energy and the diffusion time.

Polarimetric data of SN 1987A collected by Jeffery (1991) show that from day 2 to day 20 the U band polarization is about 0.2%, and the B, V, R, I band polarization is roughly 0.3% with a significant scatter. For our 3D simulations of models B15-2, N20-P, W18, and W20, we approximated the asphericity of the outer layers by an ellipsoidal shape at $t^{1}_{\rm map}$ and found in Sect. 3.1 that the maximum ratio of the semiaxes is $\approx$1.06. According to Höflich (1991), this ratio results in a linear polarization of $\approx$0.2%, which is consistent with the broadband polarimetry of SN 1987A.

4. Discussion

There are two different approaches to study the peculiar SN 1987A. In the first approach, the SN event is analyzed performing special evolutionary calculations for the progenitor star and subsequent hydrodynamic simulations. It is a long and difficult process from the main-sequence progenitor star through its stellar evolution and final explosion to the SN outburst. The present paper is the first attempt to go the last two steps in the framework of neutrino-driven simulations in three dimensions

and light curve modeling. The second approach makes no use of evolutionary progenitor calculations but relies on extracting information about the internal structure of the pre-SN, the explosion energy, and the amount of radioactive ^{56}Ni from a comprehensive comparison of the extensive observational data with adequate hydrodynamic explosion models. It thus means a reverse engineering process from the observed SN outburst to the properties of the pre-SN and the SN explosion. Utrobin (2005) carried out this kind of an investigation employing a nonevolutionary pre-SN model constructed in an optimal way to reproduce the SN 1987A outburst. This optimal model has a pre-SN radius of $35\,R_\odot$, an ejecta mass of $18\,M_\odot$, an explosion energy of 1.5 B, and a total ^{56}Ni mass of $0.0765\,M_\odot$. For a comparison of this optimal model with our selected models B15-2, N20-P, W18, and W20, the density profile of the optimal pre-SN star is shown in Fig. 1, and the corresponding light curve in Fig. 11.

The good agreement between the calculated light curve of the optimal model and that observed for the first 40 days confirms our conclusion in Sect 3.4 that the serious disagreement of the light curves of models B15-2, N20-P, W18, and W20 with the observations is caused by the large radius of the available pre-SN models and the inappropriate structure of their outer layers. The more compact and different configuration of the optimal pre-SN model compared to that of the evolutionary pre-SN models B15, N20, W18, and W20 (Fig. 1) implies that all assumptions about the modification of convective mixing (Woosley et al. 1988), mass loss and convective mixing (Saio et al. 1988), and both rotation and convective mixing (Woosley et al. 1997) have failed to improve the evolutionary calculations of single stars to the required extent. The evolution of the pre-SN in a close binary during a merger with a secondary component might offer a more promising possibility to produce the needed compact configuration. It should be noted that hydrodynamic simulations of a binary merger model have already explained the formation of the mysterious triple-ring nebula surrounding SN 1987A (Morris & Podsiadlowski 2009).

The dome-like maximum of the light curve of model B15-2 fits the observations of SN 1987A much better than the other models N20-P, W18, and W20 do (Fig. 11). It is somewhat surprising that one of the first models for the BSG Sanduleak $-69°202$ (Woosley et al. 1988) gives a good result in the framework of 3D neutrino-driven simulations and light curve modeling, while the more advanced pre-SN models W18 and W20 (Woosley 2007; Woosley et al. 1997, respectively) do less. This fact shows that the modern modifications in evolutionary calculations of single stars do not necessary mean improvements in reproducing the SN 1987A progenitor because, for the corresponding structure of the helium core and He/H composition interface, 3D neutrino-driven simulations produce insufficient amounts of outward ^{56}Ni mixing and inward hydrogen mixing.

For all models listed in Table 4, a fit of the calculated light curves in the radioactive tail to that observed implies that the total ejected mass of ^{56}Ni, on average, exceeds the observed amount of ^{56}Ni by roughly 5%. In the optimal model of SN 1987A, constructed with a nonevolutionary pre-SN model, this excess is nearly 7% (Utrobin 2007).

4.1. Assumption of spherical symmetry

In our analysis of the calculated light curves, we should keep in mind that they were obtained with the spherically symmetric radiation hydrodynamics code Crab after angular averaging of the 3D hydrodynamic flow and distribution of chemical elements. Of course, a more general and more adequate approach would be to solve the radiation hydrodynamics equations in 3D for calculating the light curves. Not applying this 3D radiation hydrodynamics solver, however, only leaves the possibility of discussing the possible influence of 3D radiation transfer on the light curve.

As shown in Sect 3.1, the outer layers of the ejecta are fairly close to a spherically symmetric flow, and the averaging procedure introduces small errors associated with the resultant 1D hydrodynamic flow and, consequently, with the calculated light curve. The small asphericity reflects the typical morphology of the hydrogen-rich outer layers, while the geometry of radioactive ^{56}Ni-rich ejecta is much more complex (Fig. 3, lower row).

The SN ejecta can be divided into the mixing zone characterized by outward mixing of ^{56}Ni and inward mixing of hydrogen, and the outer unmixed envelope, which is chemically homogeneous. The mixing zone contains a number of complex structures made of ^{56}Ni-rich matter rather than a large number of individual clumps. These ^{56}Ni structures are distributed almost homogeneously within the volume enclosed by a deformed surface, from which a few smaller, elongated structures may stick out, depending strongly on the pre-SN structure (c.f. Fig. 14 in Wongwathanarat et al. 2015). Hence, because the angular averaging of the 3D distribution of heavy elements transforms macroscopic mixing into microscopic mixing, we need to consider the influence of macroscopic mixing of ^{56}Ni-rich matter and hydrogen on the light curve.

The ^{56}Ni structures can develop into bubbles inflated by radioactive decay heating, which may result in a boost of the peak radial velocities of heavy elements. The relatively dense shell forming at the edge of this kind of bubble is Rayleigh-Taylor unstable. After $3-5$ days, the shell breaks into pieces and the ^{56}Ni-rich fragments mix with the surrounding matter (Basko 1994). Hence, radioactive decay heating enhances macroscopic mixing, tends to homogenize matter inside the mixing zone, and may modestly accelerate the ^{56}Ni-rich matter (Herant & Benz 1991; Basko 1994).

As long as the ^{56}Ni-rich ejecta remain optically thick for gamma rays, the energy from radioactive decay is deposited locally. This energy locally powers the thermal and nonthermal emissivity of matter which, in turn, forms the SN luminosity, and it tracks the original ^{56}Ni distribution until the optical depth of the ^{56}Ni-rich ejecta approaches unity (in model B15-2, for example, this happens around day 650). During the subsequent semi-transparent phase, diffusion of gamma rays smooths the complex morphology of the emissivity making it less pronounced.

4.2. Viewing angle dependence

For photons the ejecta remain optically thick from the onset of the explosion until well into the radioactive tail (in model B15-2, for example, until around day 170). During the CRW phase, up to about day 20 (Fig. 7a), the SN luminosity forms in the hydrogen-rich envelope, which is chemically homogeneous and almost spherically symmetric. By the end of the CRW phase, the photosphere is approaching the outer edge of the mixing zone and then enters the ^{56}Ni-rich ejecta where gamma rays deposit their energy locally. From this epoch on, the radioactive decay of ^{56}Ni and ^{56}Co becomes dominant in powering the luminosity. As a consequence, the luminosity becomes viewing angle dependent, while the ejecta remain optically thick for photons. Thus, the 3D morphology of thermal and nonthermal emissivity produced by the gamma-ray deposition remains unchanged when the photon luminosity is sensitive to the heterogeneity of the mixing zone.

From the end of the CRW phase (when in model B15-2, for example, the optical depth in the mixing zone is about 10^4) through the semitransparent phase (optical depth of order unity) the photosphere approaches the outer edge of the mixing zone, enters it, and eventually disappears. During this period, two important manifestations of the complex morphology of the mixing zone exist. First, because Thomson scattering by free electrons dominates the opacity, diffusing thermal and nonthermal photons cannot provide any local information, i.e., the emergent flux depends on the global properties of the mixing zone and the SN luminosity becomes viewing angle dependent.

Second, macroscopic inhomogeneities in the chemical composition and in the density distribution in the mixing zone reduce the effective opacity of matter compared to the homogeneous case, and, consequently, the characteristic diffusion time of photons. The reduced diffusion time results in a luminosity increase after the end of the CRW phase.

A closer look at the morphology of the ^{56}Ni-rich ejecta (Fig. 3, lower row) suggests that these effects could be observationally significant for model B15-2. In the other models N20-P, W18, and W20 the viewing angle effect might be less noticeable because of a closer similarity of the morphology of their ^{56}Ni-rich ejecta to a spherical distribution.

As a simple illustrative example let us consider an aspherical explosion that is strongest and leads to the most intense mixing in one direction and is weakest and leads to the least intense mixing in the opposite direction. If we are oriented to the side of the strongest explosion, we can observe the light curve with the smooth rising part similar to that of the optimal model (Fig. 11). Observations along the opposite direction, in turn, would reveal a local minimum in the light curve shortly after the end of the CRW phase like that of model B15-2, if in this hemisphere the extent of ^{56}Ni mixing turns out to be insufficient to produce the luminosity required for the smoothness of the light curve.

During both the CRW phase and the late phase when the ejecta are transparent for photons, the SN luminosity is independent of the macroscopic properties of the mixing zone. However, between these two phases a viewing angle effect is present. It first reveals itself when the photosphere is approaching the edge of the mixing zone. The effect then gradually increases as the photosphere enters the mixing zone and descends into it. The growth of the viewing angle effect is caused by the increase of the volume of the mixing zone above the photosphere. After having revealed the morphology of the mixing zone, the viewing angle effect approaches a maximum and then starts to decrease, while the mixing zone becomes more and more transparent. The behavior of the viewing angle effect should correlate with the evolution of polarization properties. It is remarkable that broadband polarimetry of SN 1987A shows a similar behavior with time (Jeffery 1991).

4.3. Ejecta

The question of the ejecta mass determination is of great importance for any SN. For SN 1987A, a well-observed and well-studied supernova, this problem becomes crucial. Generally, it would be tempting to determine the ejecta mass by means of 3D neutrino-driven simulations and light curve modeling based on evolutionary pre-SN models. A relevant evolutionary pre-SN model has to ensure a perfect fit of the hydrodynamic model to the observations of SN 1987A. Unfortunately, the lack of agreement between the calculated light curves and the observations of SN 1987A during the first 30 – 40 days does not permit us to resolve this issue using the available pre-SN models. In addition, even in the case of model B15-2, having the best dome-like maximum of the light curve, there is a deficit of luminosity during the transition from the maximum to the radioactive tail in comparison with the observed light curve (Fig. 11).

It is noteworthy that among a family of SN 1987A-like events with dome-like light curves there is a peculiar object, SN 2000cb. The latter is characterized by an explosion energy of 4.4 B and mixing of radioactive ^{56}Ni up to a velocity of 8400 km s^{-1} (Utrobin & Chugai 2011). SN 1987A and SN 2000cb show that the greater the explosion energy is, the higher is the degree of ^{56}Ni mixing. The same trend is demonstrated by models B15-1, B15-2, and B15-3 (Tables 2 and 3). In the case of model B15-3 the maximum velocity of ^{56}Ni matter is about 7300 km s^{-1} (Fig. 7d), which is comparable with that of SN 2000cb. Unfortunately, a more detailed and meaningful assessment of this SN seems to be questionable in the framework of neutrino-driven explosions because the explosion energy of 4.4 B for SN 2000cb may be hard to reach with explosions driven by the neutrino-heating mechanism (Ugliano et al. 2012).

The important observation of a high-velocity clump of $\sim 10^{-3}\,M_\odot$ with a speed of about 4700 km s^{-1} in the envelope of SN 1987A (Utrobin et al. 1995) is not reproduced by any of our investigated models with SN 1987A-like explosion energies (see Sect. 3.4 and Table 3), also, in particular, not by model B15-2. Also, a modest increase of the explosion energy does not remove this discrepancy because the maximum ^{56}Ni velocities scale roughly and moderately with the square root of the explosion energy (Wongwathanarat et al. 2015).

4.4. Progenitors

Comparing the observational data of the BSG Sanduleak −69°202 and evolutionary stellar models, Saio et al. (1988) and Woosley (1988) concluded that the star, at the time of its explosion, had a helium-core mass of $\approx 6\,M_\odot$. From an inspection of Table 1, it is evident that only pre-SN models N20 and W20 have helium-core masses consistent with the above estimate. Unfortunately, using these models in our 3D neutrino-driven simulations results in mixing of ^{56}Ni that is too weak and, as a consequence, in a disagreement of the calculated light curves with the observations of SN 1987A (Fig. 11). Thus, a correct mass of the helium core in the pre-SN configuration does not guarantee an adequate explanation of the SN 1987A phenomenon. In this context, a helium-core mass of 4.08 $M_\odot$ in the pre-SN model B15 appears as a serious shortcoming to fit the observational data of the BSG Sanduleak −69°202. This conclusion seems in line with our finding (Sect. 3.4) that the deficit of model B15-2 in matching the late-time light curve of SN 1987A can only be cured by an increase of the ejecta mass and a proportional increase of the explosion energy.

The 3D simulations we employed started from spherically symmetric progenitor models. To initiate the growth of nonradial hydrodynamic instabilities, small seed perturbations had been imposed as zone-to-zone variations of the radial velocity with chosen amplitude in the whole computational domain at the start of the 3D simulations shortly after core bounce. However, Arnett & Meakin (2011, see also references in their paper) pointed out that turbulent convective shell burning might produce large-scale precollapse asphericity in the progenitor core, and, in particular, of the O-burning shell, which could affect explosion asymmetries, neutron-star kicks, and nickel mixing during the explosion. In addition, Couch & Ott (2013) showed that the revival of the stalled SN shock by neutrino heating could be triggered by nonradial flows in the progenitor core because of perturbations in

the Si/O burning shells, when advected through the accretion shock, enhance nonradial mass motions and turbulent pressure in the postshock region (Couch & Ott 2015; Müller & Janka 2015). While these effects might be of relevance in the context discussed in our paper, it is unclear whether the relatively large initial perturbations that are needed to make a sizable impact are realistic (Müller & Janka 2015). A quantitatively meaningful assessment is currently not possible because the perturbation pattern and amplitude in 3D stars prior to core collapse must still be determined by multidimensional simulations of the late stages of stellar evolution.

4.5. Numerical resolution

It is unlikely that the inability of our models to reproduce the high-velocity clump observed in the envelope of SN 1987A (see Sect. 4.3) is a fundamental problem of the neutrino-driven explosion mechanism. A number of possibilities may naturally cure this deficit.

Besides possible large-scale progenitor asphericities prior to stellar core collapse (see the discussion in Sect. 4.4) and a different progenitor structure, which plays a crucial role for the long-time propagation and deceleration of the iron-group ejecta (cf. Wongwathanarat et al. 2015; Hammer et al. 2010), the most important aspect is the numerical resolution of the 3D simulations. For reasons of computational efficiency, the employed 3D models were computed with an angular resolution of only two degrees. Comparisons with one-degree simulations showed good agreement in the distribution and motion of the bulk of nickel, but the amount and speed of the fastest radioactive ^{56}Ni turned out to be highly sensitive to the grid resolution. Both the amount and speed of the fastest ^{56}Ni decrease with time as the flow expands over the Eulerian grid (Wongwathanarat et al. 2015). These effects are undesirable artificial, but unavoidable consequences of numerical viscosity and diffusivity, which become more serious for coarser resolution. In a 3D explosion simulation of our considered B15 progenitor with similar explosion energy, Hammer et al. (2010) obtained maximum ^{56}Ni velocities of up to 4500 km s^{-1}, which is in the ballpark of the fastest radioactive material observed in SN 1987A. This simulation employed a regular spherical polar grid and thus had higher spatial (linear) resolution in the azimuthal direction near the polar axis than the best models of Wongwathanarat et al. (2015) with their Yin-Yang grid. The result of Hammer et al. (2010) demonstrates that it is well possible to retain nickel at speeds considerably above 4000 km s^{-1} in the B15 model with explosion energies around 1 − 1.5 B.

5. Conclusions

Comparing results of 3D neutrino-driven simulations and light curve modeling with the observations of SN 1987A allows us to draw the following principal conclusions, which, of course, depend on the considered set of pre-SN models:

- The dome of the light curve of model B15-2 for the late-time 1D simulation agrees with the observations of SN 1987A much better than that of the other models N20-P, W18, and W20 (Fig. 11). There is only one defect in the dome shape – a deficit of the luminosity during the transition from the maximum to the radioactive tail.
- To fit the observations in the radioactive tail, we adjusted the ejected amount of ^{56}Ni, taking fallback of radioactive ^{56}Ni starting from the onset of light curve modeling into account (Table 4). The required initial ^{56}Ni masses in the early- and late-time 1D simulations fall in between the minimum and maximum estimates obtained in our 3D explosion models, implying that all 3D neutrino-driven simulations under study are able to synthesize the ejected amount of radioactive ^{56}Ni.
- The analysis of SN 1987A observations revealed the fact that radioactive ^{56}Ni was mixed in the ejecta up to a velocity of about 3000 km s^{-1}. Only models B15-1 and B15-2 yield a maximum velocity of the bulk of ^{56}Ni consistent with the observations, with ^{56}Ni being concentrated around a velocity of about 1000 km s^{-1} (Table 3, Figs. 7b and c).
- In hydrodynamic models W18 and W20, fallback of the radioactive ^{56}Ni is not negligible (Table 4).
- Our set of pre-SN models provides the opportunity to study the sensitivity of outward ^{56}Ni mixing and inward hydrogen mixing to the structure of the helium core and the He/H composition interface. It turned out that mixing of radioactive ^{56}Ni in velocity space and the average mass fraction of mixed hydrogen $\langle X \rangle$ decreased, while the mass of hydrogen mixed into the He shell did not show any systematics in the sequence of models B15-2, N20-P, W18, and W20 with comparable explosion energies (Table 3).
- It is remarkable that in all models hydrogen mixing, occurring during the 3D neutrino-driven simulations, results in minimum velocities of hydrogen-rich matter of less than 100 km s^{-1}, which is in a good agreement with the spectral observations of SN 1987A.

In addition, we can summarize a few secondary findings:

– The influence of the chemical composition of the hydrogen-rich envelope on the mixing of radioactive ^{56}Ni and hydrogen was studied with model N20-P ($X_{\rm surf}$ = 0.56) and the additional model N20-C ($X_{\rm surf}$ = 0.735). This increase of the hydrogen abundance from that of the pre-SN to the LMC-typical value does not affect the mixing of radioactive ^{56}Ni and only slightly increases the hydrogen mass fraction in the mixing zone (Table 3).
– Mixing between $t^{\rm e}_{\rm map}$, prior to shock breakout, and $t^{\rm l}_{\rm map}$, long after shock breakout when the ejecta expand almost homologously, increases both the mass fraction of hydrogen in the metal core and that of radioactive ^{56}Ni in the outer part of the mixing zone, with the maximum ^{56}Ni velocity remaining unchanged (Fig. 6).
– Models B15-1, B15-2, and B15-3 demonstrate that the greater the explosion energy (Table 2), the more intense is the mixing of radioactive ^{56}Ni in velocity space, the greater is the average mass fraction of mixed hydrogen $\langle X \rangle$, and the higher is the mass of hydrogen mixed into the He shell (Table 3).

We conclude with some critical comments about the pre-SN models for SN 1987A, which we used in our 3D neutrino-driven simulations and light curve modeling. Common shortcomings of all pre-SN models studied are a pre-SN radius that is too large to fit the initial luminosity peak of SN 1987A and a structure of the outer layers that is inadequate to match the observed light curve during the first 40 days. At the same time, the structure of the helium core and of the He/H composition interface in the pre-SN model B15 facilitates the production of a sufficient amount of outward ^{56}Ni mixing and of inward hydrogen mixing in model B15-2 and, as a consequence, results in a dome-like maximum of the light curve that fits the observations much better than the maxima of the other models do. Unfortunately, a helium-core mass of 4.08 $M_\odot$ in the pre-SN model B15 is in conflict with

observational data of the BSG Sanduleak −69°202. Therefore, there is no evolutionary pre-SN model with the required helium-core mass of $6\,M_\odot$ and a suitable structure of the helium core and He/H composition interface. The lack of an adequate pre-SN model for the well-observed and well-studied SN 1987A is a real and pressing challenge for the stellar evolution theory of massive stars. An important lesson from our study of SN 1987A is that the evolutionary picture for the late stages of massive stars may require revision in ways yet to be determined.

Finally, we state that the available pre-SN models, self-consistent 3D neutrino-driven simulations, and light curve modeling can explain the basic observational data of SN 1987A, except for those related to the detailed pre-SN structure of the outer layers, within the paradigm of the neutrino-driven explosion mechanism.

Acknowledgements. We would like to thank Ken Nomoto and Stan Woosley for providing us with the pre-SN data. V.P.U. was supported by the guest program of the Max-Planck-Institut für Astrophysik. At Garching, funding by the Deutsche Forschungsgemeinschaft through grants SFB/TR7 "Gravitational Wave Astronomy" and EXC 153 "Origin and Structure of the Universe" and by the EU through ERC-AdG No. 341157-COCO2CASA is acknowledged. Computation of the 3D models and postprocessing of the data were done on Hydra of the Rechenzentrum Garching.

References

Arcones, A., Janka, H.-T., & Scheck, L. 2007, A&A, 467, 1227
Arnett, D., Fryxell, B., & Müller, E. 1989, ApJ, 341, L63
Arnett, W. D. 1979, ApJ, 230, L37
Arnett, W. D. 1987, ApJ, 319, 136
Arnett, W. D. & Meakin, C. 2011, ApJ, 733, 78
Basko, M. 1994, ApJ, 425, 264
Bell, K. L. & Berrington, K. A. 1987, Journal of Physics B Atomic Molecular Physics, 20, 801
Blinnikov, S., Lundqvist, P., Bartunov, O., Nomoto, K., & Iwamoto, K. 2000, ApJ, 532, 1132
Burrows, A. 2013, Reviews of Modern Physics, 85, 245
Burrows, A. & Fryxell, B. A. 1993, ApJ, 418, L33
Burrows, A., Hayes, J., & Fryxell, B. A. 1995, ApJ, 450, 830
Burrows, A. & van Riper, K. A. 1995, ApJ, 455, 215
Caramana, E. J., Shashkov, M. J., & Whalen, P. P. 1998, Journal of Computational Physics, 144, 70
Cassatella, A. 1987, in European Southern Observatory Conference and Workshop Proceedings, Vol. 26, European Southern Observatory Conference and Workshop Proceedings, ed. I. J. Danziger, 101–110
Castor, J. I., Abbott, D. C., & Klein, R. I. 1975, ApJ, 195, 157
Catchpole, R. M., Menzies, J. W., Monk, A. S., et al. 1987, MNRAS, 229, 15P
Catchpole, R. M., Whitelock, P. A., Feast, M. W., et al. 1988, MNRAS, 231, 75P
Chevalier, R. A. 1989, ApJ, 346, 847
Chugai, N. N. 1991, Soviet Ast., 35, 171
Colella, P. & Glaz, H. M. 1985, Journal of Computational Physics, 59, 264
Colella, P. & Woodward, P. R. 1984, Journal of Computational Physics, 54, 174
Colgan, S. W. J., Haas, M. R., Erickson, E. F., Lord, S. D., & Hollenbach, D. J. 1994, ApJ, 427, 874
Couch, S. M. & Ott, C. D. 2013, ApJ, 778, L7
Couch, S. M. & Ott, C. D. 2015, ApJ, 799, 5
Ellinger, C. I., Young, P. A., Fryer, C. L., & Rockefeller, G. 2012, ApJ, 755, 160
Falk, S. W. & Arnett, W. D. 1977, A&AS, 33, 515
Fischer, T., Whitehouse, S. C., Mezzacappa, A., Thielemann, F.-K., & Liebendörfer, M. 2010, A&A, 517, A80
Fröhlich, C., Martínez-Pinedo, G., Liebendörfer, M., et al. 2006, Physical Review Letters, 96, 142502
Fryxell, B., Arnett, D., & Müller, E. 1991, ApJ, 367, 619
Gaensler, B. M., Staveley-Smith, L., Manchester, R. N., et al. 2007, in American Institute of Physics Conference Series, Vol. 937, Supernova 1987A: 20 Years After: Supernovae and Gamma-Ray Bursters, ed. S. Immler, K. Weiler, & R. McCray, 86–95
Gavrila, M. 1967, Physical Review, 163, 147
Gear, C. W. 1971, Numerical initial value problems in ordinary differential equations
Grassberg, E. K., Imshennik, V. S., & Nadyozhin, D. K. 1971, Ap&SS, 10, 28
Grassberg, E. K. & Nadyozhin, D. K. 1976, Ap&SS, 44, 429
Haas, M. R., Erickson, E. F., Lord, S. D., et al. 1990, ApJ, 360, 257
Hachisu, I., Matsuda, T., Nomoto, K., & Shigeyama, T. 1990, ApJ, 358, L57
Hachisu, I., Matsuda, T., Nomoto, K., & Shigeyama, T. 1991, ApJ, 368, L27
Hachisu, I., Matsuda, T., Nomoto, K., & Shigeyama, T. 1992, ApJ, 390, 230
Hachisu, I., Matsuda, T., Nomoto, K., & Shigeyama, T. 1994, A&AS, 104, 341
Hairer, E., Nørsett, S. P., & Wanner, G. 1993, Solving Ordinary Differential Equations I, Nonstiff Problems, second revised edn. (Springer-Verlag Berlin Heidelberg)
Hairer, E. & Wanner, G. 1996, Solving Ordinary Differential Equations II, Stiff and Differential-Algebraic Problems, second revised edn. (Springer-Verlag Berlin Heidelberg)
Hammer, N. J., Janka, H.-T., & Müller, E. 2010, ApJ, 714, 1371
Hamuy, M., Suntzeff, N. B., Gonzalez, R., & Martin, G. 1988, AJ, 95, 63
Handy, T., Plewa, T., & Odrzywołek, A. 2014, ApJ, 783, 125
Hanuschik, R. W. & Dachs, J. 1987, A&A, 182, L29
Hauschildt, P. H. & Baron, E. 2014, A&A, 566, A89
Heger, A., Fryer, C. L., Woosley, S. E., Langer, N., & Hartmann, D. H. 2003, ApJ, 591, 288
Herant, M. & Benz, W. 1991, ApJ, 370, L81
Herant, M. & Benz, W. 1992, ApJ, 387, 294
Herant, M., Benz, W., & Colgate, S. 1992, ApJ, 395, 642
Herant, M., Benz, W., Hix, W. R., Fryer, C. L., & Colgate, S. A. 1994, ApJ, 435, 339
Herant, M. & Woosley, S. E. 1994, ApJ, 425, 814
Hillebrandt, W., Höflich, P., Weiss, A., & Truran, J. W. 1987, Nature, 327, 597
Hillebrandt, W. & Meyer, F. 1989, A&A, 219, L3
Höflich, P. 1991, A&A, 246, 481
Hungerford, A. L., Fryer, C. L., & Warren, M. S. 2003, ApJ, 594, 390
Imshennik, V. S. & Nadezhin, D. K. 1989, Astrophysics and Space Physics Reviews, 8, 1
Irwin, A. W. 1981, ApJS, 45, 621
Iwamoto, K., Young, T. R., Nakasato, N., et al. 1997, ApJ, 477, 865
Janev, R. K., Langer, W. D., & Evans, K. 1987, Elementary processes in Hydrogen-Helium plasmas - Cross sections and reaction rate coefficients
Janka, H.-T. 2012, Annual Review of Nuclear and Particle Science, 62, 407
Janka, H.-T., Hanke, F., Hüdepohl, L., et al. 2012, Progress of Theoretical and Experimental Physics, 2012, 010000
Janka, H.-T. & Müller, E. 1996, A&A, 306, 167
Jeffery, D. J. 1991, ApJS, 77, 405
Kageyama, A. & Sato, T. 2004, Geochemistry, Geophysics, Geosystems, 5, 9005
Kane, J., Arnett, D., Remington, B. A., et al. 2000, ApJ, 528, 989
Kasen, D., Thomas, R. C., & Nugent, P. 2006, ApJ, 651, 366
Khokhlov, A. M., Höflich, P. A., Oran, E. S., et al. 1999, ApJ, 524, L107
Kifonidis, K., Plewa, T., Janka, H.-T., & Müller, E. 2000, ApJ, 531, L123
Kifonidis, K., Plewa, T., Janka, H.-T., & Müller, E. 2003, A&A, 408, 621
Kifonidis, K., Plewa, T., Scheck, L., Janka, H.-T., & Müller, E. 2006, A&A, 453, 661
Kozma, C. & Fransson, C. 1992, ApJ, 390, 602
Kozma, C. & Fransson, C. 1998, ApJ, 497, 431
Kurucz, R. L. 2002, in American Institute of Physics Conference Series, Vol. 636, Atomic and Molecular Data and Their Applications, ed. D. R. Schultz, P. S. Krstic, & F. Ownby, 134–143
Li, H., McCray, R., & Sunyaev, R. A. 1993, ApJ, 419, 824
Liou, M. 1996, Journal of Computational Physics, 129, 364
Lundqvist, P. & Fransson, C. 1996, ApJ, 464, 924
Mezzacappa, A., Calder, A. C., Bruenn, S. W., et al. 1998, ApJ, 495, 911
Mihalas, D. & Mihalas, B. W. 1984, Foundations of radiation hydrodynamics
Miller, D. S., Wilson, J. R., & Mayle, R. W. 1993, ApJ, 415, 278
Morris, T. & Podsiadlowski, P. 2009, MNRAS, 399, 515
Müller, B. & Janka, H.-T. 2015, MNRAS, 448, 2141
Müller, B., Janka, H.-T., & Marek, A. 2012a, ApJ, 756, 84
Müller, E., Fryxell, B., & Arnett, D. 1991a, in European Southern Observatory Conference and Workshop Proceedings, Vol. 37, European Southern Observatory Conference and Workshop Proceedings, ed. I. J. Danziger & K. Kjaer, 99
Müller, E., Fryxell, B., & Arnett, D. 1991b, A&A, 251, 505
Müller, E., Janka, H.-T., & Wongwathanarat, A. 2012b, A&A, 537, A63
Müller, E. & Steinmetz, M. 1995, Computer Physics Communications, 89, 45
Nagataki, S., Hashimoto, M.-A., Sato, K., & Yamada, S. 1997, ApJ, 486, 1026
Nagataki, S., Shimizu, T. M., & Sato, K. 1998, ApJ, 495, 413
O'Connor, E. & Ott, C. D. 2011, ApJ, 730, 70
Phillips, M. M., Hamuy, M., Heathcote, S. R., Suntzeff, N. B., & Kirhakos, S. 1990, AJ, 99, 1133
Phillips, M. M. & Heathcote, S. R. 1989, PASP, 101, 137
Pinto, P. A. & Woosley, S. E. 1988, ApJ, 329, 820
Plewa, T. & Müller, E. 1999, A&A, 342, 179
Podsiadlowski, P. & Joss, P. C. 1989, Nature, 338, 401
Pruet, J., Hoffman, R. D., Woosley, S. E., Janka, H.-T., & Buras, R. 2006, ApJ, 644, 1028
Quirk, J. J. 1994, International Journal for Numerical Methods in Fluids, 18, 555
Saio, H., Nomoto, K., & Kato, M. 1988, Nature, 334, 508

Scheck, L., Kifonidis, K., Janka, H.-T., & Müller, E. 2006, A&A, 457, 963
Shigeyama, T., Iwamoto, K., Hachisu, I., Nomoto, K., & Saio, H. 1996, in IAU Colloq. 145: Supernovae and Supernova Remnants, ed. T. S. Kuhn, 129
Shigeyama, T. & Nomoto, K. 1990, ApJ, 360, 242
Smartt, S. J. 2009, ARA&A, 47, 63
Strang, G. 1968, SIAM Journal on Numerical Analysis, 5, 506
Sukhbold, T. & Woosley, S. E. 2014, ApJ, 783, 10
Sutherland, R. S. 1998, MNRAS, 300, 321
Sutherland, R. S. & Dopita, M. A. 1993, ApJS, 88, 253
Tamborra, I., Hanke, F., Janka, H.-T., et al. 2014, ApJ, 792, 96
Teachout, R. R. & Pack, R. T. 1971, Atomic Data, 3, 195
Timmes, F. X. & Swesty, F. D. 2000, ApJS, 126, 501
Ugliano, M., Janka, H.-T., Marek, A., & Arcones, A. 2012, ApJ, 757, 69
Utrobin, V. P. 1989, Soviet Astronomy Letters, 15, 42
Utrobin, V. P. 1993, A&A, 270, 249
Utrobin, V. P. 2004, Astronomy Letters, 30, 293
Utrobin, V. P. 2005, Astronomy Letters, 31, 806
Utrobin, V. P. 2007, A&A, 461, 233
Utrobin, V. P. & Chugai, N. N. 2002, Astronomy Letters, 28, 386
Utrobin, V. P. & Chugai, N. N. 2005, A&A, 441, 271
Utrobin, V. P. & Chugai, N. N. 2011, A&A, 532, A100
Utrobin, V. P., Chugai, N. N., & Andronova, A. A. 1995, A&A, 295, 129
Verner, D. A., Ferland, G. J., Korista, K. T., & Yakovlev, D. G. 1996, ApJ, 465, 487
Verner, D. A. & Yakovlev, D. G. 1995, A&AS, 109, 125
Voronov, G. S. 1997, Atomic Data and Nuclear Data Tables, 65, 1
Wang, L., Wheeler, J. C., Höflich, P., et al. 2002, ApJ, 579, 671
Weiss, A., Hillebrandt, W., & Truran, J. W. 1988, A&A, 197, L11
Weymann, R. 1966, ApJ, 145, 560
Wheeler, J. C., Meier, D. L., & Wilson, J. R. 2002, ApJ, 568, 807
Wishart, A. W. 1979, MNRAS, 187, 59P
Wongwathanarat, A., Hammer, N. J., & Müller, E. 2010a, A&A, 514, A48
Wongwathanarat, A., Janka, H.-T., & Müller, E. 2010b, ApJ, 725, L106
Wongwathanarat, A., Janka, H.-T., & Müller, E. 2013, A&A, 552, A126
Wongwathanarat, A., Müller, E., & Janka, H.-T. 2015, A&A, 577, A48
Woosley, S. & Janka, T. 2005, Nature Physics, 1, 147
Woosley, S. E. 1988, ApJ, 330, 218
Woosley, S. E. 2007, private communication
Woosley, S. E., Heger, A., Weaver, T. A., & Langer, N. 1997, arXiv:astro-ph/9705146
Woosley, S. E., Pinto, P. A., & Ensman, L. 1988, ApJ, 324, 466
Yamada, S. & Sato, K. 1990, ApJ, 358, L9
Yamada, S. & Sato, K. 1991, ApJ, 382, 594